EFFECT OF PROPELLANT MORPHOLOGY ON THE ACOUSTICS OF THE BATES
MOTOR

BY

ANDREW M. NEVILL

THESIS

Submitted in partial fulfillment of the requirements
for the degree of Master of Science in Mechanical Engineering
in the Graduate College of the
University of Illinois at Urbana-Champaign, 2010

Urbana, Illinois

Advisers:

Professor Thomas L. Jackson
Professor Jonathan B. Freund

Abstract

This study shows the results of three-dimensional simulations of the chamber flow within the BATES (Ballistic Test and Evaluation System) 15 pound motor. The injection boundary conditions for the motor are defined by the velocity-temperature temporal correlations. Three different propellant morphologies are modeled and tested along with a random white noise model that represents the current surrogate for propellant modeling. The data gained from each of these simulations is compared using contour plots of the chamber flow characteristics and by performing FFT analysis on the head-end pressure histories.

The study is then expanded to include analysis of the 70 pound version of the BATES motor. The analysis of one of the propellant morphologies used in the study of the smaller motor and the white noise surrogate confirm the results of the 15 pound motor. Analysis of the acoustics and the characteristics of the chamber flow correspond with what was previously found. The results from these comparisons show that propellant morphology has a significant effect on the internal chamber flow dynamics.

Acknowledgements

There are many people who have helped me to get this thesis written. I would first like to thank my adviser, Dr. Thomas Jackson who has given me plenty of advice, helpful ideas, and proofreading assistance in addition to teaching me about acoustics and solid propellant rockets. I would also like to thank my co-adviser Dr. Jonathan Freund for looking over my results and writing and for guidance through the graduate school process. I also owe a thank you to Dr. Fady Najjar who introduced me to solid rockets and helped teach me the basics of computational fluid dynamics and how to run Rocflo. I also received many hours of help with Rocfire and with other computer problems from Victor Topalian. Finally, I would like to thank my parents and family for their support throughout this whole experience.

Table of Contents

1 Introduction

1.1 Problem Overview

Controlling the chamber flow dynamics of a solid rocket motor is an important factor in maintaining the safety and the performance of the rocket. This proves to be a difficult problem to accurately simulate; however, the Center for Simulation of Advanced Rockets (CSAR) at the University of Illinois has created a structured grid, three-dimensional flow solver that is operational for relatively short burn times.

A solid rocket motor is a rocket that uses a solid propellant, known as the grain, as its source of fuel. The propellant that is used for these rockets consists of a mixture of ammonium perchlorate (AP) and solid aluminum (Al) along with a polymeric binder. Typical composition of a solid propellant is about 88% by weight AP and Al while the other 12% is formed by the binder. Modern propellants can contain up to 30% of Al by total mass [1]. The AP acts as an oxidizer that reacts with the aluminum as the rocket is being burned. As the aluminum is burned, it creates aluminum oxide smoke (Al_2O_3) providing large amounts of heat that increase the specific impulse provided by the rocket [2]. The Al also starts to melt as it is burned, forming puddles of liquid Al that are injected into the accelerating flow. The size of these droplets of liquid Al can vary in size from a few microns to a few hundred microns, and it has been shown that the as the droplets increase in size, the burning of Al becomes more inefficient [1]. Other than the propellant, other parts commonly found in a solid rocket motor include a nozzle, igniter, casing, and thermal inhibitors that separate the rocket chamber into segments.

Solid rocket motors are used in a variety of situations because of their simplicity and because they are easier to store for long periods of time than liquid fuel rockets. Their applications include military and commercial considerations as well as space shuttle flight. One of the drawbacks of solid fuel motors, which may also be present in liquid rocket motors, is combustion instability that causes oscillations in the chamber characteristics of the motor. This is a recurring problem that has been observed and studied in a wide variety of solid rocket motor applications over the last 60 years [3]. The pressure oscillations can have an effect on both the safety of the motor and the

performance of the motor. High amplitude pressure oscillations can cause stress on the motor structure and may also cause thrust oscillations.

One such cause for the instabilities that can be found in solid rocket motors is the process of vortex shedding. According to Telara *et al.* [4], three different types of vortices can be produced. The obstacle vortex is created by intrusions into the chamber flow like a thermal inhibitor that delineates the segments of a motor. Initially, this was thought to be the solitary reason for which vortices were produced within a solid rocket motor. However, it was shown that it is possible to have vortex shedding without the presence of an obstruction in the flow chamber [5]. A parietal vortex is a vortex that is shed from near the propellant surface and is due to instabilities in the mean velocity profile that couple with acoustic frequencies within the flow chamber. This type of vortex is prevalent in the aft end of motors that have a large length dimension. The final vortex, the angle vortex, is produced by angles in the geometry of the grain.

It has been shown that instabilities grow in amplitude as the frequency of vortex shedding moves toward the frequency of the acoustic modes that are a result of the geometry of the rocket chamber [6]. Early attempts to numerically simulate the phenomenon of this acoustic mode amplification were two-dimensional studies using the unsteady Euler and Navier-Stokes equations [7]. Over time, the investigation into the role that coupling between acoustic modes and the vortex shedding frequency play in motor instability has become more complex. To increase accuracy, turbulence models have become an addition to solid rocket motor simulations. For example, Kourta used a first order turbulence model to study the interaction between vortex shedding and acoustic modes, and it was found that the turbulence model improved the prediction of flow instability in regards to both frequencies and amplitude of the oscillations [8]. The use of turbulence models in simulations has expanded so that they can now be used with fluid injection to predict parietal vortex shedding [9]. Recent studies on the effects of turbulence models in channels with injected flow have revealed that the large eddy simulation is a more accurate model than the κ-ε model, when used to simulate turbulent flow [10].

Although major advancements have been made in studying the instabilities within the chamber of a solid rocket motor, very little attention has been given to creating a

computational model of the propellant. Most studies simply use a constant mass flow rate and temperature as the injection conditions [11]. Another common surrogate for a propellant model is to use random white noise to describe the mass flow rate. However, this has proven to be an ineffective method, as shown by Apte and Yang [12] who had to impose 90% white noise on the mass flow rate to match experimental conditions.

Although propellant models are not often used in solid rocket simulations, the propellant morphology has been known to be a factor in motor instabilities. For example, it is well known that large head-end pressure oscillations leading to motor instability occurred in the 1960's Maverick program at the Army's Redstone Arsenal, which was subsequently reduced by changing the morphology of the propellant while maintaining the same burning rate [13]. The observation of changing the morphology to reduce or eliminate motor instability is usually attributed to acoustic instability that arises between the coupling of the combustion process of the solid propellant and the chamber flow dynamics [14][15]. However, recent numerical computations by Massa et al. [16] suggest an alternative or additional mechanism, that of fluctuations arising from the unsteady burning of a solid composite propellant morphology that affect the chamber flow dynamics and head-end pressure oscillations. The fact that heterogeneous propellants burn in a non-homogeneous fashion has also been confirmed experimentally [17].

An early attempt to describe propellant combustion modeling was made by Beckstead, Derr, and Price [18]. Although this was critical to exposing many important observations about how propellant combustion works, its scope was only one-dimensional. As knowledge about propellant combustion improved, a code was developed that has the ability to emulate the combustion of heterogeneous propellants [19]. This code utilizes a random packing algorithm, initially created by Knott *et al.* [20] and subsequently extended by Kochevets *et al.* [21] and Maggi *et al.* [22], which can be used to pack various sized spheres into periodic cubes. These spheres are used to approximate AP particles, and by matching the size distribution and the volume fraction of AP to that of the actual propellant, a computational model is formed. It is not realistic to expect the code to be able to resolve all sizes of the AP spheres, so the spheres that are

too small to resolve numerically are solved by a homogenization strategy in which the spheres are mixed with the fuel binder to create a homogeneous blend [23].

With the tools finally in place to create an accurate heterogeneous propellant model that could be used in computer simulations, the aforementioned study by Massa *et al.* [16] has shown that the heterogeneity of the propellant does in fact have a significant effect on the characteristics of the chamber flow. Using the process described in [19] as a model for the propellant, this study focuses on describing the flow field at an intermediate distance from the propellant surface. The statistics of the temperature and the velocity field were collected and analyzed in both the length scale and the time scale. It was found the typical length scale was too small for the statistics at one grid point to have an effect on the flow field at an adjacent grid point. However, it was also determined that the time scale is such that the temporal correlations at a grid point are significant and these fluctuations extend far enough to have an effect on the chamber flow. It was shown that the head end pressure was the location at which the chamber flow is most noticeably affected, and that the data was more realistic for the modeled propellant than for a white noise surrogate model [16].

The study conducted in [24] explores the observation that the propellant morphology has significant effects on the chamber flow by testing two different propellants on a two-dimensional, nozzleless motor. The two propellants, Th200 and M24, are compared against a random white noise process serving as a surrogate model. The results confirmed the observations of [16] in showing that the white noise model consistently resulted in lower amplitudes than the modeled propellant tests. Despite agreement with past results, the study in [24] only calculated data for two-dimensional models, so it is left unclear whether the same results would hold for a three-dimensional model. The purpose of this thesis, therefore, is to further investigate the role of propellant fluctuations (in the absence of acoustic coupling) on solid rocket motor internal flow characteristics by using three-dimensional simulations.

The structure of the remainder of the paper is as follows. Section 2 contains the problem setup and information concerning the setup of the BATES motor and the propellant models. Section 3 provides an overview of the mathematical methods that were used in creating the injection boundary conditions and in analyzing the results.

Sections 4 and 5 outline and discuss the data and results from the simulations. Section 6 contains direction for future research, and Section 7 contains concluding remarks.

2 Problem Setup

2.1 BATES Motor

The Ballistic Test and Evaluation System, or the BATES solid rocket motor, was first developed by the Air Force in the early 1960s as an experimental motor that could be used for high precision ballistics testing [25]. The goal was to produce a motor that could accurately portray the performance of a full size motor with different propellants at a minimum size to reduce the amount of materials used in testing. The initial design of the motor contained 70 pounds of propellant, while later, a smaller 15 lb. motor was also developed. The smaller design was critical in studying the effects of scaling on the motor performance, and also made the testing of scarce propellants feasible [25].

Figure 1 shows a schematic of the 15 lb. motor configuration. The specific measurements for this motor and the larger 70 lb. BATES motor can be found in Table 1. The length measurement represents the distance from the head end of the motor to the nozzle throat. The speed of sound, a, is found using:

$$a = \sqrt{\gamma R T} \tag{1}$$

Also, T represents the temperature, the term γ refers to the ratio of specific heats, and R is the specific gas constant which is determined by:

$$R = \frac{c_p (\gamma - 1)}{\gamma} \tag{2}$$

Using the properties of the motor given in Table 1, the specific gas constant is found to be 293.687 (J/kg-K) for the BATES 15 lb. motor. This value is then used in (1) to determine the speed of sound. Also, as seen in Figure 1, the motor has a converging-diverging nozzle that is attached to the chamber.

The three-dimensional computational grid and a two-dimensional cut of this grid are shown in Figure 2. It contains 220,032 nonuniformily distributed cells for the 15 lb. motor, while the larger 70 lb. motor grid, not shown, yet similar in geometry, contains 619,400 cells. Grid refinement has been performed on the grids to show that the steady state head end pressure is independent of the mesh [1]. The boundary conditions that are

set for the motor are as follows: the nozzle and head end boundaries are set as no slip walls, the nozzle outlet is set at supersonic outflow, and mass rate and temperature values are set at the injection surface of the propellant. It is the mass rate and temperature at the boundaries that will be varied in the different cases depending on what propellant is being tested.

2.2 Propellant Models

Previous study has shown that the velocity-temperature correlations above the surface of a burning heterogeneous propellant are strongly affected by the propellant morphology [16]. These effects on the velocity and temperature can then affect the amplitudes of the acoustic modes within the motor chamber. The spatial microscale has been found to be on the order of millimeters, which is too small to be accurately represented by the grid used to mesh the model of the motor, and thus spatial correlations are ignored. The temporal microscale has been found to be to the order of milliseconds, and as the time step of the simulations will be on the order of milliseconds, this parameter must be accounted for in the simulation. The temporal correlations will differ depending on the morphology of the propellant.

This study focuses on three different propellant morphologies that have varying sizes of AP. Each morphology uses HTPB as the binder that holds the solid fuel together. Rocpack, a propellant packing code that has been developed at CSAR, is the program used to create virtual propellant models that simulate the different morphologies. Cross sections of these three-dimensional packs are shown in Figure 3. The propellants that are considered in this test are P82, PBMOD, and M24. P82 is a polydisperse monomodal propellant with a mean AP diameter of 82 microns. PBMOD is a bimodal propellant with mean diameters of 82 microns for the fine AP and 390 microns for the coarser AP. The M24 is a trimodal propellant with diameters of 20 microns, 50 microns, and 200 microns. It should be kept in mind that these numbers represent mean diameters, and in actuality, the diameter of the spheres has a distribution that can be seen in Figure 4. Further details of the packs can be found in the paper by Jackson and Buckmaster [19]. In the current turbulent flow simulations, a nominal propellant model of 10% random white noise is often used in place of a propellant, so this model is also studied as a

comparison to the heterogeneous propellants. In addition to the white noise surrogate, a control model is also tested in which the injected mass rate and temperature values are fixed.

The temporal correlations that are created for each of the propellant models are described by a normally distributed joint pdf. The time sequence that is generated for each propellant is created to match statistics that have been calculated for each propellant. This time sequence must correspond with the autocovariance, the cross-covariance, and the joint pdf of the velocity and temperature correlations. The covarinace matrix that is used to describe the correlations spans a shorter time than the time required for the simulation. Therefore predictions of future correlations must be created so that they also match the statistics that were calculated.

2.3 Rocfire

Rocfire is a computer program that was developed to aid in the analysis of burning heterogeneous propellants. It is a sub-grid combustion model that can describe the coupling of the solid phase and gas phase physics at the microscale level. Rocfire uses the packed propellant cube that is generated by Rocpack and defined by the different propellants being studied as an input. Thus, the results are a function of which propellant is designated to be burned. The final result of a Rocfire simulation is the creation of temperature and velocity data from planes at a given location above the propellant surface. This data is recorded in the form of a matrix with dimensions given by the dimension of the grid used in Rocfire. The location of these planes is determined by the user, and the code is capable of creating results for multiple locations. Each of these data files also represents an instant in time, so that one matrix represents the velocity or temperature at a set position and fixed time.

Initially, Rocfire is run using the Oseen approximation which describes a viscous and incompressible flow at low Reynolds numbers. Once a steady state is reached using the Oseen solver, the Navier Stokes equations are then used to provide the data which is to be saved.

2.4 Rocflo

Rocflo is a 3-D flow solver that has been developed at CSAR that is used to find the solution to the Euler or Navier-Stokes equations. It also has the ability to include turbulence solutions using large eddy simulations. Rocflo is used as a structured grid solver, while another Rocstar program, Rocflu, must be used for unstructured grids. It can be used jointly with other Rocstar applications; however, since fluid flow is the main concern of this project, Rocflo was operated in its stand alone capacity.
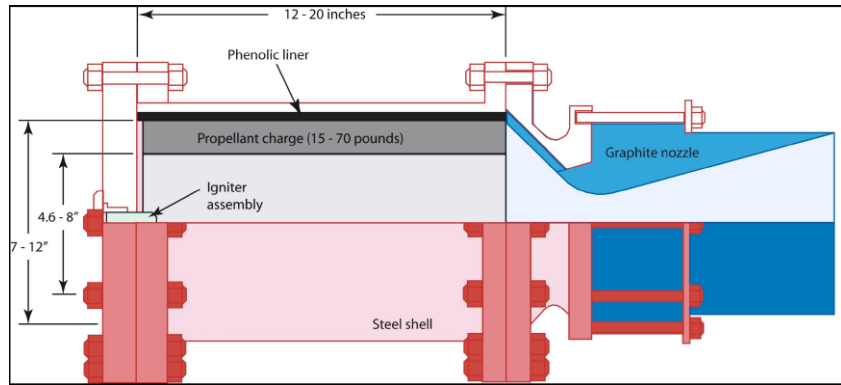
2.5 Figures and Tables

Figure 1: Schematic of the BATES motor, 15 lbs. or 70 lbs.

Table 1: Table of values for the BATES motor.

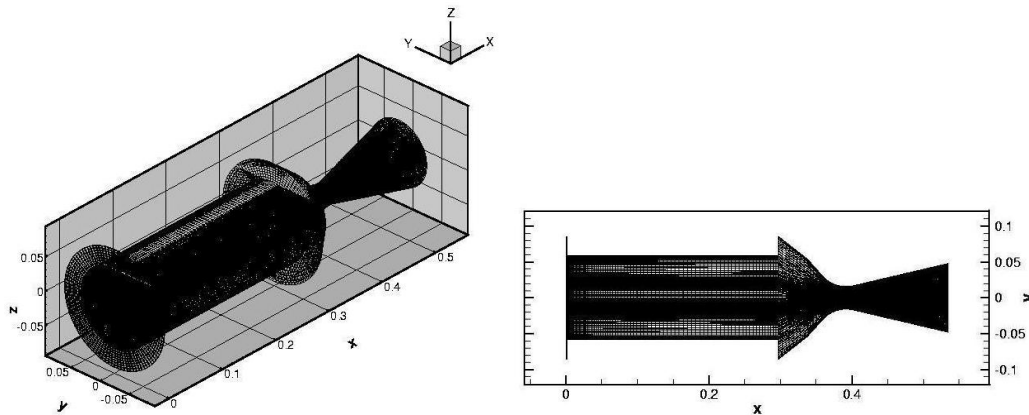| Parameter	15 lb	70 lb
L (m)	0.39	0.669
R (m)	0.05842	0.100
a (m/s)	998.3	1090
$\dot{m}$ (kg/m2-s)	22.623	27.638
T_b (K)	2876	3430
c_p (J/kg-K)	1925.28	1925.28
γ	1.18	1.18

Figure 2: Computational grid for BATES 15 lb. motor. (a) 3-D mesh. (b) 2-D mesh, slice taken at z = 0 plane.
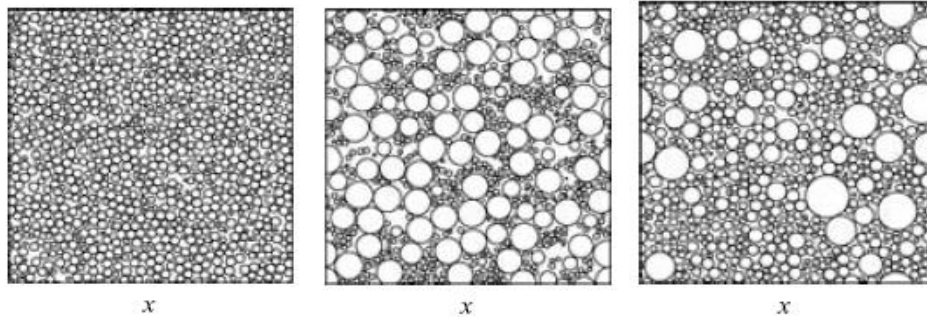
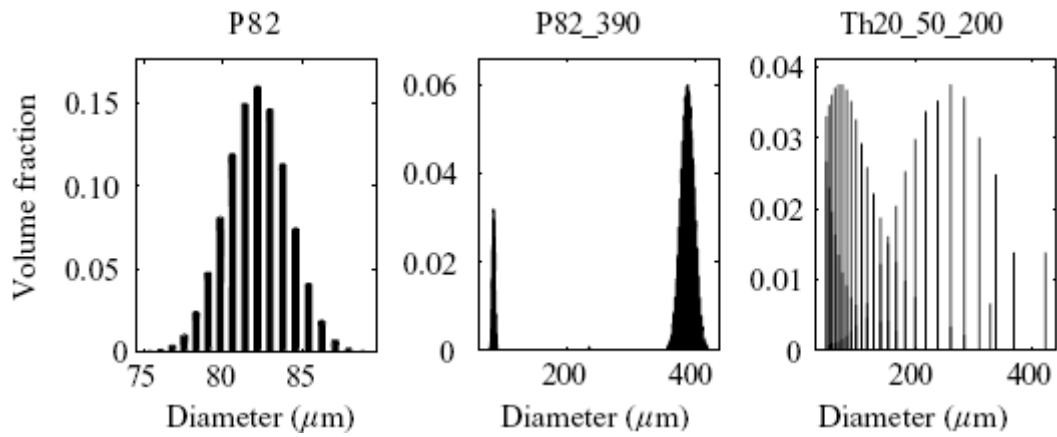**Figure 3: Cross-sectional cut of the propellant packs. (a) P82 (b) PBMOD (c) M24.**

Figure 4: Particle size distributions for (a) P82 (b) PBMOD (c) M24.

3 Mathematical Methods

3.1 Statistics

The results gathered from Rocfire are used to form the stochastic boundary conditions that are used to emulate the desired propellant morphology. Therefore, it is necessary to define which statistics are needed, and how they are calculated.

Each plane above the propellant surface is split into a grid with grid points in the x and z direction, where the grid points in x can be defined by $i = 0,1,\ldots,nx$ and the gridpoints in z can be defined as $k = 0,1,\ldots,nz$. This gives a total of (nx+1)*(nz+1) points for each grid. The y direction is defined as the height above the propellant surface and denoted by $j = 0,1,\ldots,ny$. Each plane also has different time levels where the total number of levels is given by the value of nt. Rocfire creates a data file for an X-Z plane for each y value and for each time step. Each X-Z plane data file contains either the velocity or the temperature value at every grid point. These data files are stored so that there is a time step of 0.00001s between each plane.

There are a few statistics that can be calculated for the velocity and the temperature values that are important for defining the propellant morphologies. A useful tool in studying the velocity and temperature output is a probability density function (pdf). This is a graphical tool that shows the probability that the velocity or temperature is at a certain value. A pdf is a continuous function, but the data that is recorded by Rocfire is given at distinct time steps and grid points. This problem is solved by observing that a pdf is a smoothed version of a histogram. It can be approximated using an algorithm that separates the velocity and temperature values into bins according to value. As the size of each of the bins decreases, the approximation of the pdf as a continuous function improves.

The pdf is important for determining the statistics of the propellant model. As an example, given that a set of values is represented by X and x represents a single value from the set, the pdf can be used to find the moment of the distribution using the equation below:

$$\mu_r = \int_{-\infty}^{+\infty}(x - \mu)^r \, pdf(x)dx \qquad (3)$$

The μ in the above equation is the first moment of X and is known as the expectation or the mean of the distribution. This value is integrating the product of each possible value and its probability. This idea is represented by the following equation [26]:

$$\mu = E(X) = \int_{-\infty}^{+\infty} x \cdot pdf(x)dx \tag{4}$$

This value can also be represented in discrete form:

$$\mu = E(X) = \sum_{x} xP(x) \tag{5}$$

The second moment is more commonly known as the variance of the distribution and is a measure of the spread or the dispersion of the data points x from the mean. Thus, the equation for the variance in terms of the expectation is given by [26]:

$$Var(X) = \sigma^2 = \int_{-\infty}^{+\infty} (x - \mu)^2 pdf(x)dx \tag{6}$$

The second moment can also be found in terms of the expectation by letting r = 2 for (3):

$$Var(X) = \sigma^2 = E(X - \mu)^2 \tag{7}$$

The standard deviation of the distribution, σ, is calculated by finding the square root of the variance.

The third moment of the distribution X represents its skewness. This is a measure of the symmetry of a distribution. Similarly to the second moment found above, the third moment can be found by letting r = 3 in (3):

$$\tau = \int_{-\infty}^{+\infty} (x - \mu)^3 pdf(x)dx \tag{8}$$

It is possible to find the values for each of these terms for both the temperature and the velocity calculated in Rocfire.

The fact that there are two different distributions being considered, velocity and temperature, necessitates the need to look at the joint probability density function for these variables. A joint pdf describes the probability of events occurring in terms of two random variables X and Y. This distribution does not give specific information regarding the probabilities for just X or just Y. This information can be found from a marginal distribution, for example, the marginal distribution of X describes the probability distribution of X while ignoring all information about Y. It is possible to recover a marginal distribution from any joint pdf; however, a joint pdf can only be formed from a

marginal distribution in a certain case. If the variables X and Y are independent, then the joint pdf may be formed by multiplying the two distributions. Independence may be determined if X and Y follow the below equation:

$$P(X,Y) = P(X)P(Y) \tag{9}$$

For the problem being studied in this paper, it is assumed that the variables are not independent, that velocity and temperature are correlated. In the discrete form, the joint pdf for v and T is found in a similar method as for the marginal distributions where an algorithm separates values into bins depending on value.

It is possible to show that the velocity and the temperature may be approximated to be normally distributed as shown in Figure 5. Although this is not a determining condition for whether the joint pdf also has a normal distribution, it does make a normal joint pdf possible. It would be difficult to calculate the exact joint pdf for this case; however, the assumption that it would have a normal distribution seems plausible. Therefore, the normal joint distribution of velocity and temperature is determined from their univariate distributions, rather than the usual method of finding the marginal distributions from the joint pdf.

3.2 Covariance Matrix

The velocity and temperature data that is created from Rocfire varies depending on the model of propellant that is used as an input. The data that results from the Rocfire simulation is used to compute a covariance matrix that Rocflo uses to set the injection boundary conditions on the motor.

There are several assumptions that are used when creating the covariance matrix. First, the process is assumed to be stationary, inferring that the joint probabililty function will be constant regardless of the time or space at which it is calculated. Second, it is also assumed that there is a correlation between velocity and the temperature; these are not independent variables. Last, the velocity and temperature have approximately normal probability densities, so it is assumed that the joint pdf is also normal.

The covariance matrix holds four different data entries for each time. Two of the entries are calculations of the covariance between velocity and temperature. The

covariance between two sets of data, X and Y, is a moment of the joint distribution of X and Y which shows the direction of their relationship [26].

$$\text{cov}(X,Y) = E\big[(X_i - \mu_x)(Y_i - \mu_y)\big] \tag{10}$$

In terms of Rocfire output, X and Y are represented as the temperature and the velocity. If the temperature and velocity are positively related, then covariance will be positive. If the two data sets are negatively related then the covariance will be negative. If the velocity and the temperature are independent, then the covariance would be equal to zero. One of the covariance matrix entries is the value of cov(v,T) while another is the value of cov(T,v) at the given time. These values should be equal because the covariance is found through multiplication, and the commutative property shows that the order of the variables is unimportant.

The other two entries in the covariance matrix are a specific type of covariance calculation where a signal is compared to a time shifted portion of itself. This is known as the autocovariance of a signal. In mathematical form, the autocovariance is defined as:

$$\gamma(i, j) = E\big[(X_i - \mu_i)(X_j - \mu_j)\big] \tag{11}$$

where X is the time signal, μ is the mean, and i and j represent different periods of time sampled from that signal. This definition can change when it is assumed that the time signal is stationary, implying that the mean is the same regardless of what period of time is taken from the time series. Stationarity assumes that μ_i and μ_j are equal, so the equation for autocovariance becomes:

$$\gamma(k) = E\big[(X_i - \mu)(X_{i-k} - \mu)\big] \tag{12}$$

where k refers to the time lag between the two sampled times rather than the specific time periods denoted by i and j.

The values for the covariance and the autocovariance of the velocity and temperature data is then used to create a covariance matrix, which has the following definition,

$$\Sigma = E\big[(\vec{y} - \vec{\mu})(\vec{y} - \vec{\mu})^T\big] \tag{13}$$

in which the vector y is an ordered pair (v_m, T_m) for the given time step m. The fluctuation, $(\vec{y} - \vec{\mu})$, will be referred to as $\vec{Y}$. This vector will have a number of values that is defined by the number of time steps.

$$\vec{Y} = \left(v'(0), T'(0), v'(\Delta t), T'(\Delta t), v'(2\Delta t), T'(2\Delta t), ..., v'(nt\Delta t), T'(nt\Delta t)\right) \qquad (14)$$

The definition of the covariance matrix can now be simplified to

$$\Sigma = E\left[\vec{Y}\vec{Y}^{T}\right] \qquad (15)$$

This formula yields a matrix that has the following form.

V(0)v(0)	v(0)T(0)	v(0)v(Δt)	v(0)T(Δt)	...	v(0)v(ntΔt)	v(0)T(ntΔt)
V(0)T(0)	T(0)T(0)	v(Δt)T(0)	T(0)T(Δt)	...	v(ntΔt)T(0)	T(0)T(ntΔt)
V(0)v(Δt)	v(Δt)T(0)	v(Δt)v(Δt)	V(Δt)T(Δt)	...	v(Δt)v(ntΔt)	v(Δt)T(ntΔt)
v(0)T(Δt)	T(0)T(Δt)	v(Δt)T(Δt)	T(Δt)T(Δt)	...	v(ntΔt)T(Δt)	T(Δt)T(ntΔt)
⋮	⋮	⋮	⋮	⋯	⋮	⋮
v(0)v(ntΔt)	v(ntΔt)T(0)	V(Δt)v(ntΔt)	V(Δt)T(ntΔt)	...	v(ntΔt)v(ntΔt)	v(ntΔt)T(Δt)
v(0)T(ntΔt)	T(0)T(ntΔt)	V(Δt)T(ntΔt)	T(Δt)T(ntΔt)	...	v(ntΔt)T(ntΔt)	T(ntΔt)T(Δt)

The matrix shown above is simplified so that only the difference between the time steps in the two terms is used.

vv(0)	vT(0)	vv(Δt)	vT(Δt)	...	vv(ntΔt)	vT(ntΔt)
vT(0)	TT(0)	vT(0)	TT(Δt)	...	vT(0)	TT(ntΔt)
vv(Δt)	vT(0)	vv(Δt)	vT(Δt)	...	vv(ntΔt)	vT(ntΔt)
vT(Δt)	TT(Δt)	vT(Δt)	TT(Δt)	...	vT(Δt)	TT(ntΔt)
⋮	⋮	⋮	⋮	⋯	⋮	⋮
Vv(ntΔt)	vT(0)	vv(ntΔt)	vT(ntΔt)	...	vv(ntΔt)	vT(Δt)
vT(ntΔt)	TT(ntΔt)	vT(ntΔt)	TT(ntΔt)	...	vT(ntΔt)	TT(Δt)

The covariance matrix Σ can be observed to be symmetric; therefore, it may be stored as an upper triangular matrix in order to reduce the amount of computer memory required for storage. These values are then stored in the .cov file as a matrix that has two columns. The result is the covariance file that is used in the directory from which the simulations are being run.

$$
\begin{vmatrix}
vv(0) & vT(0) \\
Tv(0) & TT(0) \\
vv(\Delta t) & vT(\Delta t) \\
Tv(\Delta t) & TT(\Delta t) \\
\vdots & \vdots \\
vv(nt\Delta t) & vT(nt\Delta t) \\
Tv(nt\Delta t) & TT(nt\Delta t)
\end{vmatrix}
$$

An algorithm within the Rocflo code has been constructed that can reconstruct this 2 column vector into the upper triangular matrix that is the original covariance matrix.

The size of the matrix in the .cov file depends on the length of the Rocfire run. There are always 2 columns, but the number of rows is free to change depending on the number of time steps that were calculated in Rocfire. If the number of rows in the covariance matrix is represented by the variable ncovvals, then the total time can be found by the equation shown below

$$
\frac{n\mathrm{cov}vals}{2} - 1 = nt \tag{16}
$$

The total time can be found using the time step value, Δt, so the equation above can be modified to be:

$$
t_{total} = \Delta t \left(\frac{n\mathrm{cov}vals}{2} - 1 \right) \tag{17}
$$

This equation can also be inverted to determine the dimensions of the covariance matrix when the Rocfire simulation time is known.

$$
n\mathrm{cov}\,vals = 2 \left(\frac{t_{total}}{\Delta t} + 1 \right) \tag{18}
$$

The result is the recovery of ncovvals, the number of rows that will be present in the covariance matrix.

3.3 Acoustics

The Navier-Stokes equations can be used to describe the flow of a fluid, resulting in a solution of the fluid's velocity field. These equations are three-dimensional and

represent the conservation of mass, momentum, and energy. In their full form, the Navier-Stokes equations prove difficult to work with; however, in studying the acoustics of the flow through the chamber of the BATES motor they may be simplified by making some assumptions. First, the flow is assumed to be inviscid without having any heat conduction. The result is the Euler equations shown below. When the isentropic relation between pressure and density is included with the Euler equations, the system is closed and may be solved.

Mass:

$$\frac{\partial \rho}{\partial t} + \nabla \bullet (\rho \bar{u}) = 0 \tag{19}$$

Momentum:

$$\frac{\partial \rho \bar{u}}{\partial t} + \nabla \bullet (\bar{u} \otimes \rho \bar{u}) + \nabla p = 0 \tag{20}$$

Isentropic Gas Law:

$$p = A\rho^\gamma \tag{21}$$

The meaning for the variables in the above equations is as follows. The term ρ stands for the density, t is the time, $\bar{u}$ is the velocity vector, p is the pressure, A is a constant, ∇ is a spatial operator used for the divergence and gradient, and γ represents the ratio between the specific heats.

The flow is also assumed to be one-dimensional, in so that it only moves in the downstream x direction. This allows the terms with y, z, v, and w to be dropped because these values will be equal to zero. This also means that the y and z direction momentum equations can be disregarded. This results in the one-dimensional Euler equations for mass and x-momentum as shown below,

Mass:

$$\rho_t + (\rho u)_x = 0 \tag{22}$$

x-momentum:

$$(\rho u)_t + (\rho u^2)_x + p_x = 0 \tag{23}$$

Now that the Navier-Stokes equations have been simplified using the assumptions given to the flow, the induced fluctuations must be taken into account. The fluctuation terms are taken to be very small compared to the mean value. It may also be assumed that the mean velocity, $\bar{u}$, is small so that it can be approximated as zero. Also, the mean values are taken to be constant in both time and space, so the partial derivatives of the means will be equal to zero. These simplifications allow the density, velocity, and pressure terms to be written as a sum of their steady state value and the fluctuation.

$$\rho = \bar{\rho} + \rho' \tag{24a}$$

$$p = \bar{p} + p' \tag{24b}$$

$$u = \bar{u} + u' \tag{24c}$$

The terms with the bar over the variable represent the steady state value while the primed terms are the fluctuation from the mean. These new expressions for the density, pressure, and velocity can be substituted into the one-dimensional Euler equations, (22) and (23), resulting in the equations given below.

Mass:

$$\rho'_t + \bar{\rho} u'_x = 0 \tag{25}$$

Momentum:

$$\bar{\rho} u'_t + p'_x = 0 \tag{26}$$

To get to these equations, the non-linear terms were neglected because the multiplication of two fluctuations can be ignored since $|p' p'| << |p'|$.

The relation between the pressure and the density must also be put in terms of the mean and fluctuation values. The resulting equation is

$$\bar{p} + p' = A(\bar{\rho} + \rho')^\gamma \tag{27}$$

By removing the $\bar{\rho}$ from the parentheses on the right side of (27), this may be rewritten as

$$\bar{p} + p' = A\bar{\rho}\left(1 + \frac{\rho'}{\bar{\rho}}\right)^{\gamma} \tag{28}$$

The right side of (28) can be expanded into a Taylor series to give

$$\bar{p} + p' = A\bar{\rho}\left(1 + \frac{\gamma\rho'}{\bar{\rho}} + \left(\gamma^2 - \gamma\right)\left(\frac{\rho'}{\bar{\rho}}\right)^2 + \ldots\right) \tag{29}$$

where the higher order terms may be ignored because they become increasingly small. Now, it is useful to only consider the first two terms of the expansion and to multiply through by the mean density term.

$$\bar{p} + p' = A\bar{\rho}^{\gamma} + A\bar{\rho}^{\gamma}\frac{\gamma\rho'}{\bar{\rho}} \tag{30}$$

If it is assumed that the mean values of pressure and density follow the relation that was shown in (23), then, with some rearrangement of terms, (30) gives an equation to find the density fluctuation.

$$\rho' = \left(A\gamma\bar{\rho}^{\gamma-1}\right)^{-1} p' \tag{31}$$

There are now three simplified equations that will be used, (25), (26), and (31). The next step is to take the derivative of (25) in time and the derivative of (26) in space.

$$\rho'_{tt} + \bar{\rho}u'_{xt} = 0 \tag{32}$$

$$\bar{\rho}u'_{xt} + p'_{xx} = 0 \tag{33}$$

These two equations may be combined into a single equation using substitution when it is noticed that the term $\bar{\rho}u'_{xt}$ is in each (32) and (33).

$$\rho'_{tt} - p'_{xx} = 0 \tag{34}$$

This equation only contains terms for the density and the pressure. The goal is to find an equation that only contains the pressure, so (31) may be used to turn the density fluctuation into a term that contains the pressure fluctuation.

$$p'_{tt} - A\frac{\gamma\bar{\rho}^{\gamma}}{\bar{\rho}} p'_{xx} = 0 \tag{35}$$

It is possible to simplify the coefficient that is found in front of p'_{xx}. For an isentropic flow, the speed of sound is given by:

$$a^2 = \frac{\gamma \bar{p}}{\bar{\rho}} \qquad (36)$$

When the relation between pressure and density from (23) is applied, this equation becomes

$$a^2 = \frac{A\gamma\bar{\rho}^{\gamma}}{\bar{\rho}} \qquad (37)$$

This result shows that the square of the sound speed is equal to the coefficient found in (35). There is now a partial differential equation that depends only on the speed of sound and the pressure.

$$p'_{tt} - a^2 p'_{xx} = 0 \qquad (38)$$

Since this partial differential equation is linear, the method of separation of variables may be used to find the solution. Separation of variables is based on the fact that the solution to (38) can be determined by a product of two functions. One of the functions relies only on the time, t, and the other relies only on the position, x.

$$p'(x,t) = T(t)X(x) \qquad (39)$$

This solution may then be substituted into (38),

$$T''(t)X(x) - a^2 T(t)X''(x) = 0 \qquad (40)$$

This equation may be rewritten after dividing by X(x) and T(t). The result is that the functions of T and X are separated.

$$\frac{T''(t)}{T(t)} - a^2 \frac{X''(x)}{X(x)} = 0 \qquad (41)$$

The only way for the difference between these two terms to be equal to zero is for $\dfrac{T''(t)}{T(t)}$

and $a^2 \dfrac{X''(x)}{X(x)}$ to be equal to a constant value. Since it does not matter what this constant value is as long as it is the same for each term, it may be represented arbitrarily by the symbol α. To make solving the differential equation easier, this constant will be squared and made negative, so that the result is:

$$\frac{T''(t)}{T(t)} = -\alpha^2 \quad \text{and} \quad \frac{X''(t)}{X(t)} = -\frac{\alpha^2}{a^2} \qquad (42)$$

These two equations can be rearranged to be in the form of homogeneous ordinary differential equations that can be solved.

$$T''(t) + \alpha^2 T(t) = 0 \tag{43a}$$

$$X''(x) + \frac{\alpha^2}{a^2} X(x) = 0 \tag{43b}$$

The solution to the equations (43a) and (43b) are shown below.

$$T = C_1 \cos(\alpha t) + C_2 \sin(\alpha t) \tag{44a}$$

$$X = C_3 \cos(\frac{\alpha}{a} x) + C_4 \sin(\frac{\alpha}{a} x) \tag{44b}$$

The coefficients are constant values that are denoted by a C with a subscript.

It would be easy to set the values of the unknown constants and the value of α to be zero to make a solution that is viable. However, this solution, as will be shown, is not useful in finding the frequencies of the acoustic modes. When α is zero, equations (43a) and (43b) become

$$T''(t) = 0 \tag{45a}$$

$$X''(x) = 0 \tag{45b}$$

When these values are integrated, they become

$$T(t) = C_1 t + C_2 \tag{46a}$$

$$X(x) = C_3 x + C_4 \tag{46b}$$

Boundary conditions must be known to be able to solve for the constants. In the case of pressure in a motor that acts like a closed-closed tube, the boundary conditions of the derivative of the pressure fluctuation equation due to position (44b) can be determined. The pressure gradient fluctuation at the head end of the motor where x = 0, and the pressure gradient fluctuation at the throat of the nozzle where x = L are both zero. This can be proven by looking at (26). At the closed end of the tube the velocity is zero because the flow cannot move through the wall. This means that the velocity fluctuation u'_t must have a value of zero. Also, the spatial gradient of the pressure, p'_x, must also equal zero to satisfy (26). Letting $X'(0) = 0$ makes the constant C_3 equal to zero. It is also assumed that the initial condition of the system is $T(0) = 0$. This boundary condition

makes the constant C_2 equal to zero. Two of the constants have now been solved and the resulting equations are,

$$T(t) = C_1 t \tag{47a}$$

$$X(x) = C_4 \tag{47b}$$

When these values are put into (39) it becomes,

$$p'(x,t) = Ct \tag{48}$$

Although this is a correct solution to the equation, it does not contain sine or cosine terms that would describe the acoustic modes. Therefore, the term α should be considered to be a nonzero value.

To find a useful solution, equations (44a) and (44b) will be used again, but with the condition that α is not zero. Since two boundary conditions are known for the derivative of (44b), it serves as a good starting point for determining the unknown coefficients. The derivative is shown below:

$$X'(x) = -C_3 \frac{\alpha}{a} \sin(\frac{\alpha}{a} x) + C_4 \frac{\alpha}{a} \cos(\frac{\alpha}{a} x) \tag{49}$$

The closed-closed tube boundary conditions for pressure gradients can then be substituted into (36) to find the values of the coefficients C_3 and C_4.

$$X'(0) = 0 = -C_3 \frac{\alpha}{a} \sin(\frac{\alpha}{a}(0)) + C_4 \frac{\alpha}{a} \cos(\frac{\alpha}{a}(0)) \tag{50}$$

For this equation, the sine term is equal to zero. Therefore, to satisfy the boundary condition, the coefficient C_4 must be equal to zero because α/a and the cosine term are nonzero. The position equation can now be simplified to become the following.

$$X'(x) = -C_3 \frac{\alpha}{a} \sin(\frac{\alpha}{a} x) \tag{51}$$

Now, the second boundary condition, $X'(L) = 0$, may be used.

$$X'(L) = 0 = -C_3 \frac{\alpha}{a} \sin(\frac{\alpha}{a}(L)) \tag{52}$$

For a non-trivial solution, the coefficient C_3 cannot be set to zero. Therefore, since α/a is known to be nonzero, the sine term must be equal to zero. This implies,

$$0 = \sin(\frac{\alpha}{a}(L)) \tag{53}$$

Since multiples of π make a sine equal to zero,

$$\frac{\alpha}{a}L = n\pi \qquad\qquad n = 1,\ 2,\ 3,\ \dots \qquad\qquad (54)$$

Solving for the constant α results in,

$$\alpha = \frac{n\pi a}{L} \qquad\qquad n = 1,\ 2,\ 3,\ \dots \qquad\qquad (55)$$

The determined values for C_3 and C_4 can be inserted into (44b) to find a solution for X(x). The unknown constant C_3 in (52) may be set to any value other than zero as long as α is chosen as the value shown above. To make this equation as simple as possible, C_3 can be chosen to equal 1.

$$X = \cos(\frac{\alpha}{a}x) \qquad\qquad\qquad (56)$$

This solution may be substituted into equation (39) to provide a solution to the spatial part of the pressure fluctuation.

$$p'(x,t) = T(t)\cos(\frac{\alpha}{a}x) \qquad\qquad\qquad (57)$$

Now, a solution for the time part of the fluctuation, T(t), must be found. It is known that the time dependent portion of the pressure fluctuation is represented by (44a). At the initial time when t = 0, the pressure gradient should still be zero. Therefore, the coefficient C_1 must be zero. The equation now becomes,

$$T = C_2 \sin(\alpha t) \qquad\qquad\qquad (58)$$

To make the solution easier to obtain, let the coefficient C2 be equal to one.

$$T = \sin(\alpha t) \qquad\qquad\qquad (59)$$

Although, by itself, the above represents a viable solution, a useful relationship can be determined by rewriting the value of α. By setting the constant α equal to angular frequency (α = 2πf) in equation (55), it is possible to introduce the temporal frequency.

$$2\pi f = \frac{n\pi a}{L} \qquad\qquad n = 1,\ 2,\ 3,\ \dots \qquad\qquad (60)$$

When this equation is rearranged to solve for the frequency, an equation that can be used to solve for the frequency of the longitudinal modes of the motor is produced.

$$f = \frac{na}{2L} \qquad\qquad n = 1,\ 2,\ 3,\ \dots \qquad\qquad (61)$$

This equation will be used in the Results section of this paper to provide the theoretical frequencies for the pressure FFT plots.

The spatially dependent term of the above equation is a cosine function and therefore is oscillatory. The solution to this equation may be found by setting the term α to equal the angular frequency, $2\pi f$. Then when α is expanded to the form shown in (55), the value for the pressure fluctuation becomes:

$$p'(x,t) = \sin(\alpha t)\cos(\frac{n\pi x}{L}) \qquad n = 1, 2, 3, \ldots \qquad (62)$$

A plot of this graph at an instant in time and letting T(t) equal one is shown in Figure 6. This plot shows that the different modes, which are determined by the value of n in (62), have an impact on the pressure fluctuation. Of particular importance are the odd numbered modes because of the way that they affect the boundaries of the motor. The even numbered modes have an equal pressure at x = 0 and at x = L, so that the effect on the boundaries is canceled because an equal pressure is pushing in opposite directions at each boundary. However, for the odd numbered modes, at x = 0, the pressure amplitude is equal to 1, while at x = L, the pressure amplitude is equal to -1. This creates a force on the x = 0 boundary that is working in the same direction as the force that is pushing on the boundary at x = L. Therefore, this force is not cancelled and has an effect on the chamber flow of the motor. The understanding of this force is essential for the safety of manned space flight because of the potential effects that it could have on the astronauts in the space shuttle.

3.4 Waterfall Plot

Although not used in the analysis of the results for this study, a waterfall plot is another useful tool that can be used to analyze the acoustics of a motor. It can be used to visually present values across two separate variables in one plot. It is useful in acoustics as a method in which to show oscillation amplitudes in terms of time and frequency. A Matlab code can be created to compute and plot waterfall plots using the data from probe files that are generated from Rocflo. This is done using a time span of probe data and splitting this data into smaller time windows to be analyzed. These time windows generally have some overlap into the times of adjacent windows. FFT analysis is then run

on each of these time windows, so that each window has its own set of magnitudes on the frequency scale. The result is a frequency scale and a time scale, and also a magnitude that corresponds to a particular time and frequency.

Waterfall plots are also helpful in determining areas of resonance, as a resonant frequency will be exhibited as a ridge of increasing amplitude as it progresses through time. It is useful to examine an example that features resonance to be able to see the ridge created in the waterfall plot. The differential equation shown below is used as an example of a system that has resonance.

$$\frac{d^2 x}{dt^2} + \omega^2 x = F_o \sin\left(\gamma t\right) \tag{63}$$

Then, theoretical values were chosen for the variables. The variable F_o was set to be 5, the term ω was given the value $25 \cdot 2\pi$, and γ was given the value $10 \cdot 2\pi$. The term γ is the one that determines the resonance of the system where the resonant frequency in Hertz can be found using the formula $\frac{\gamma}{2\pi}$. Therefore, in this example, the resonant frequency is expected to be at 10 Hz, and this result is confirmed by the waterfall plot shown in Figure 7. There is a ridge of high amplitude at 10 Hz that continually increases as time progresses, thus indicating resonance at this frequency. As shown in the figure, the waterfall plot has gridlines for only one of the variables. When using the amplitudes from the FFT plot, it is most useful to include gridlines from constant times. This creates a collection of FFT plots that show the results at various time windows where the plotted time value is the middle of each window for which the FFT was generated.
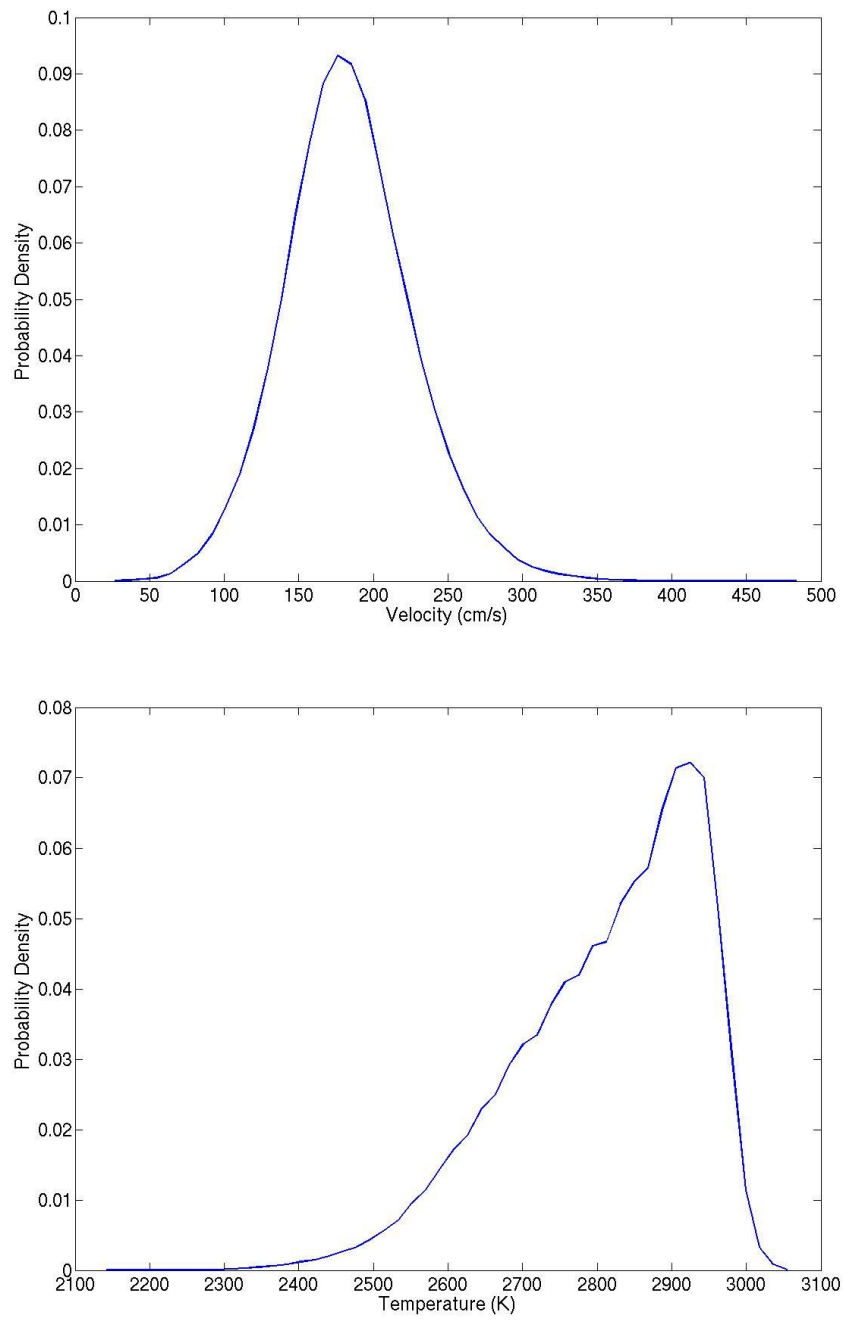
3.5 Figures

Figure 5: Velocity (top) and temperature (bottom) distributions from Rocfire output for PBMOD.
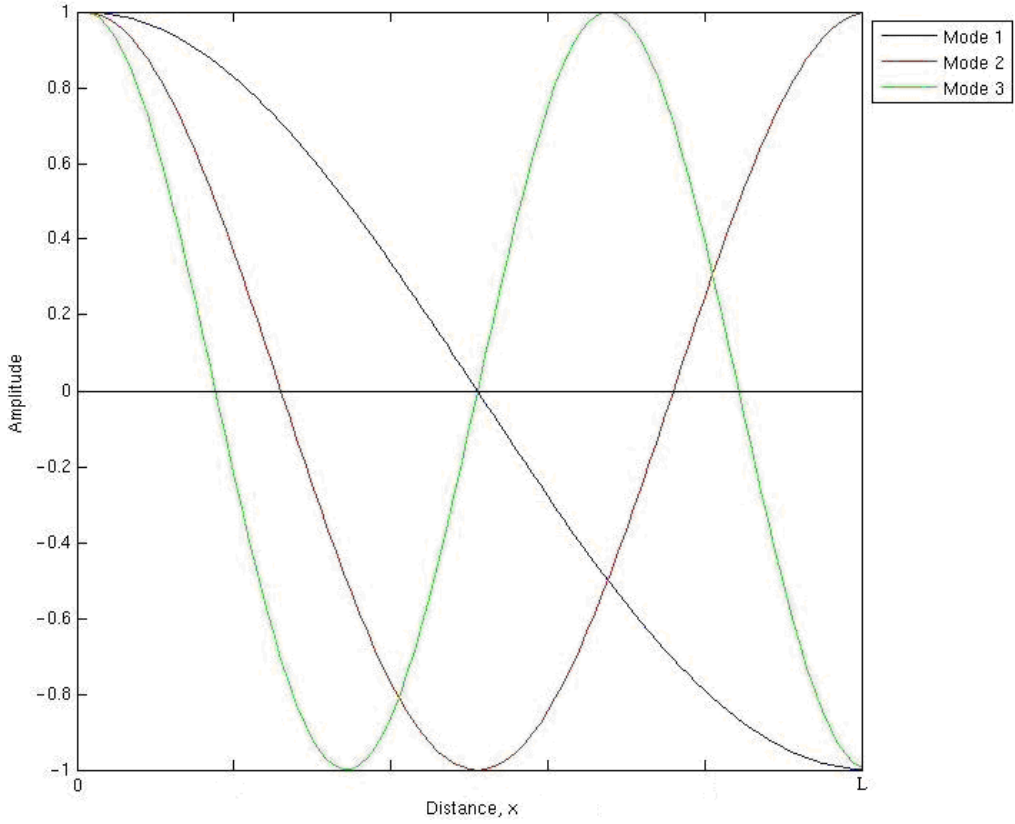
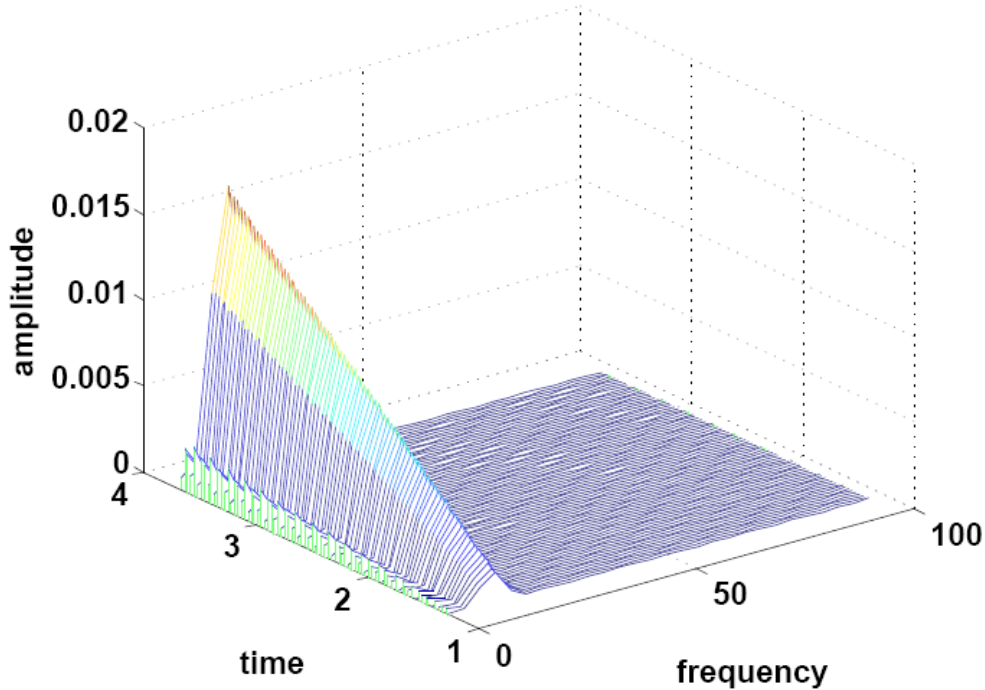**Figure 6: Plot of the acoustic modes in a motor of length of L.**

Figure 7: Waterfall plot for a system with resonance at 10 Hz.

4 Bates 15 lb. Motor Results

4.1 Acoustics

To study the longitudinal acoustic modes of the BATES 15 lb. motor it is necessary to look at the pressure history as a function of time. Figure 8 shows the head end pressure time history for the three propellant cases and also for the white noise and no fluctuations cases that were simulated. The time span of this plot is from 0.5 seconds until 1.5 seconds with a time step of 0.1ms between each data point for the propellant cases. The white noise case has a time step of 0.01ms between data points to ensure that the acoustic modes can be accurately captured. The time averages for each case in the time window displayed by Figure 8 are shown in Table 2. The head end pressure averages are shown to be similar for each case; however, each of the cases has a small difference from the case that has no fluctuations. The propellant modeled cases can have either a higher of a lower pressure average than the case without fluctuations, so there is a slight dependence on the type of propellant being used in determining the average pressure.

Other than just having a difference in the head end pressure average, the propellant model cases also show a larger variation in pressure than the white noise model. There is even a noticeable difference between each propellant as the P82 propellant has low amplitude oscillations, and the bimodal propellant, PBMOD, exhibits a large pressure change as a result of its oscillation.

The FFT plots of the head end pressure probe of the BATES 15lb. motor are shown in Figure 9. The range of these plots was made to be from 0 to 5000 Hz so that three of the longitudinal modes could be clearly captured. The theoretical and the actual values of the longitudinal modes for each of the four cases shown above are given in Table 3. The theoretical values for the longitudinal dimensional frequencies in a closed-end tube are calculated from $f* = ma/(2L)$ s^{-1}, where m denotes the mode that is being evaluated so that m = 1, 2, 3, ….

There are a few trends that can be observed from the results shown in Table 3. First, the three propellant cases and the white noise case have peaks at frequencies that are similar to the calculated theoretical mode, validating that the peaks that are evident in

the FFT plots from Figure 9 are due to the rocket acoustics. Secondly, the amplitudes for all of the cases decrease as the longitudinal mode number increases. While the three propellant cases show somewhat similar percentage loss in the amplitude of the acoustic mode, the white noise case has a less drastic decrease in amplitude. Lastly, the amplitude shows a dependence on the type of propellant that is used to set the boundary conditions. The bimodal propellant, PBMOD, always exhibits the highest amplitude, and at one point is three times greater than the amplitude of P82. The white noise case has much lower amplitude at the first acoustic mode than any of the propellant cases. It is almost four times smaller than the P82 case, which exhibits the smallest amplitude of any of the propellants. The acute differences between each of the four cases provide clear evidence that the amplitude of the longitudinal acoustic modes is affected by the propellant morphology.

4.2 Chamber Flow Dynamics

Another area of interest is the effect that propellant morphology has on the chamber flow dynamics of the BATES 15lb. motor. The plots in Figures 10–13 show the temperature contours at different instances in time for each of the three propellant cases, and also for white noise. The location of these slices is 0.2 meters downstream from the head end of the motor.

These figures show that a contrast exists between the temperature distributions in each of the four cases. The fluctuations defined by P82 produce a temperature contour that has small changes near the propellant surface, but very little effect on the interior of the chamber. The PBMOD defined boundary conditions, meanwhile, produce a temperature distribution that is not as uniform as what was found in the P82 case. The propellant surface exhibits a larger variation of temperature and the interior of the motor also shows fluctuation in the temperature values. The M24 case also shows temperature variation that is unique from what was found for the P82 and PBMOD described boundary conditions. While showing more temperature variation than P82, there is not as much variation than what is seen for PBMOD. Although the white noise boundary condition captures the temperature fluctuation near the propellant surface, it does not exhibit the same fluctuation in the chamber interior that is present in the PBMOD and

M24 cases. The differences between each of these cases show that propellant morphology has a strong influence on the chamber flow dynamics of the motor, which further points out the flaws in using white noise as a surrogate model for a heterogeneous propellant.

The plots in Figure 14 show the temperature contours for a slice taken at $z = 0$ m for each of the four cases tested with boundary condition inputs. These results are similar to what was found for Figures 10-13 where P82 shows very little temperature fluctuation and PBMOD shows the most variation in temperature. The surface of the propellant exhibits the biggest temperature changes, while the interior of the chamber has temperatures closer to the average value. The white noise and the P82 cases show very little change in the interior temperature, while M24 and PBMOD has a noticeable fluctuation in interior chamber temperature. This is further proof that the white noise model cannot be used as a reliable predictor of the chamber flow dynamics with the presence of a heterogeneous propellant.

4.3 Figures and Tables
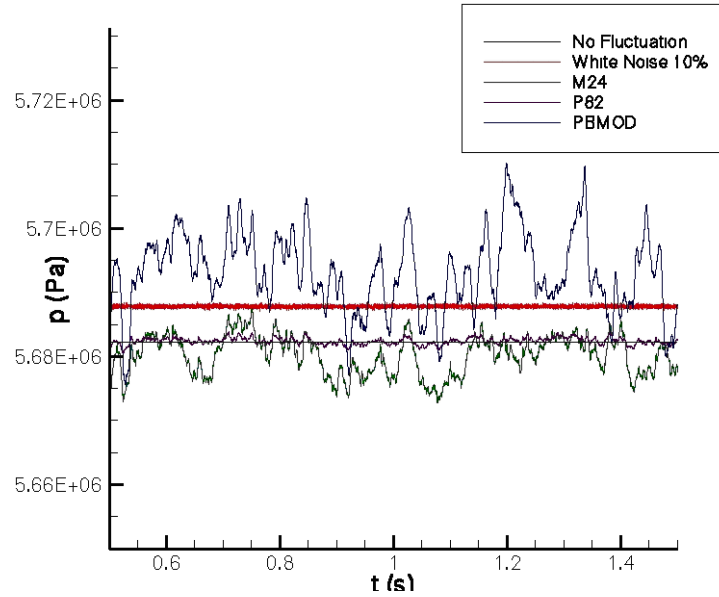
Figure 8: Time history of the head end pressure for the 15lb. BATES motor.

Table 2: Average head end pressure. Time: 0.5s - 1.5s.

Case	Average Pressure (MPa)
No Fluctuations	5.6822
White Noise	5.6878
P82	5.6824
PBMOD	5.6931
M24	5.6801

(a)   (b)

(c)   (d)
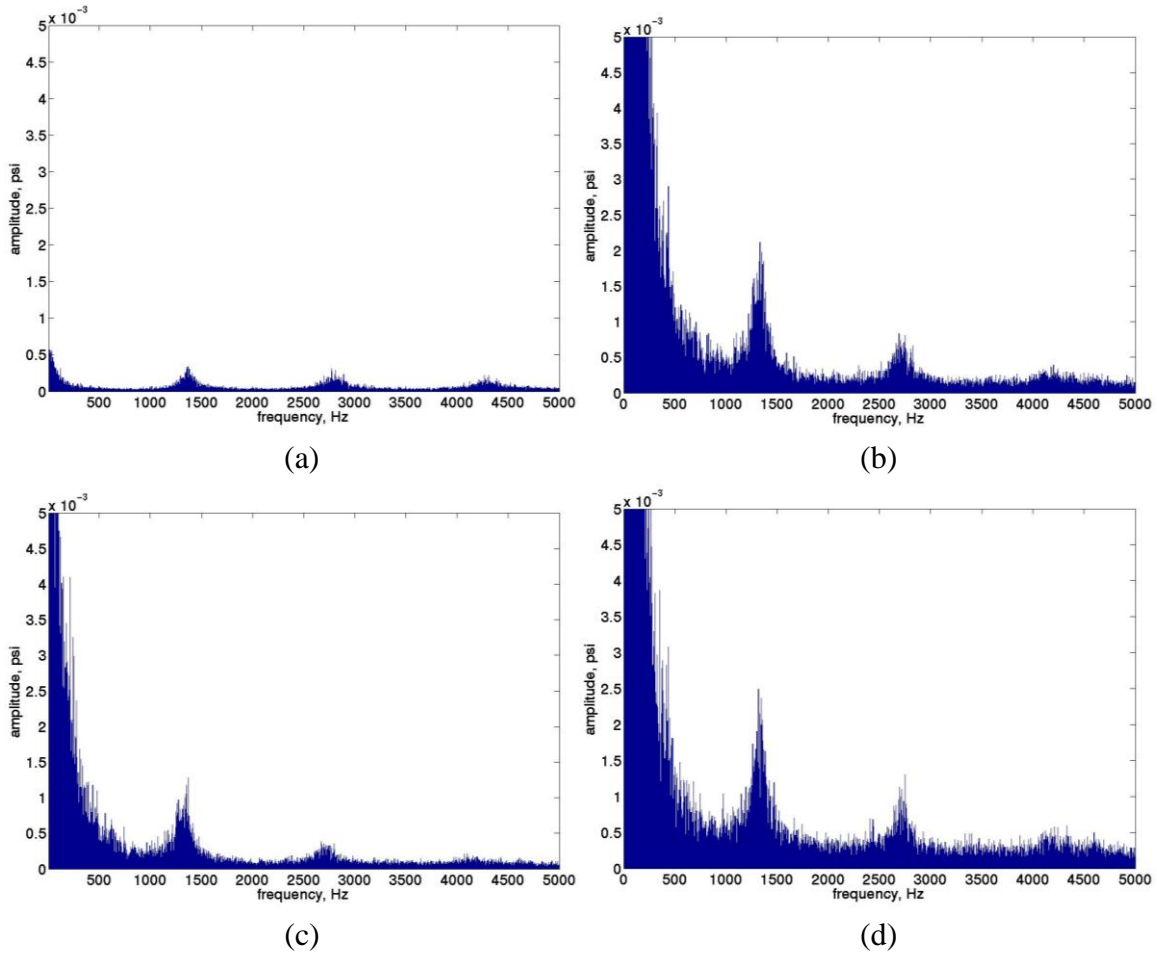
Figure 9: FFT plots at 0.5s – 1.5s for (a) White Noise 10% (b) M24 (c) P82 (d) PBMOD.

Table 3: Computed and theoretical frequencies of the first three longitudinal modes for all 5 cases studied for the Bates 15lb. motor.

Longitudinal Mode	1			2			3		
	Hz	Pa	psi	Hz	Pa	Psi	Hz	Pa	Psi
Theoretical	1280	---	---	2560	---	---	3840	---	---
White Noise	1370	2.32	0.000337	2770	2.12	0.000308	4270	1.51	0.000219
P82	1370	8.83	0.00128	2670	2.65	0.00038	4100	1.57	0.00022
PBMOD	1320	19.30	0.00280	2730	8.41	0.00122	4160	4.28	0.00062
M24	1330	15.44	0.00223	2740	5.91	0.00086	4200	3.04	0.00044
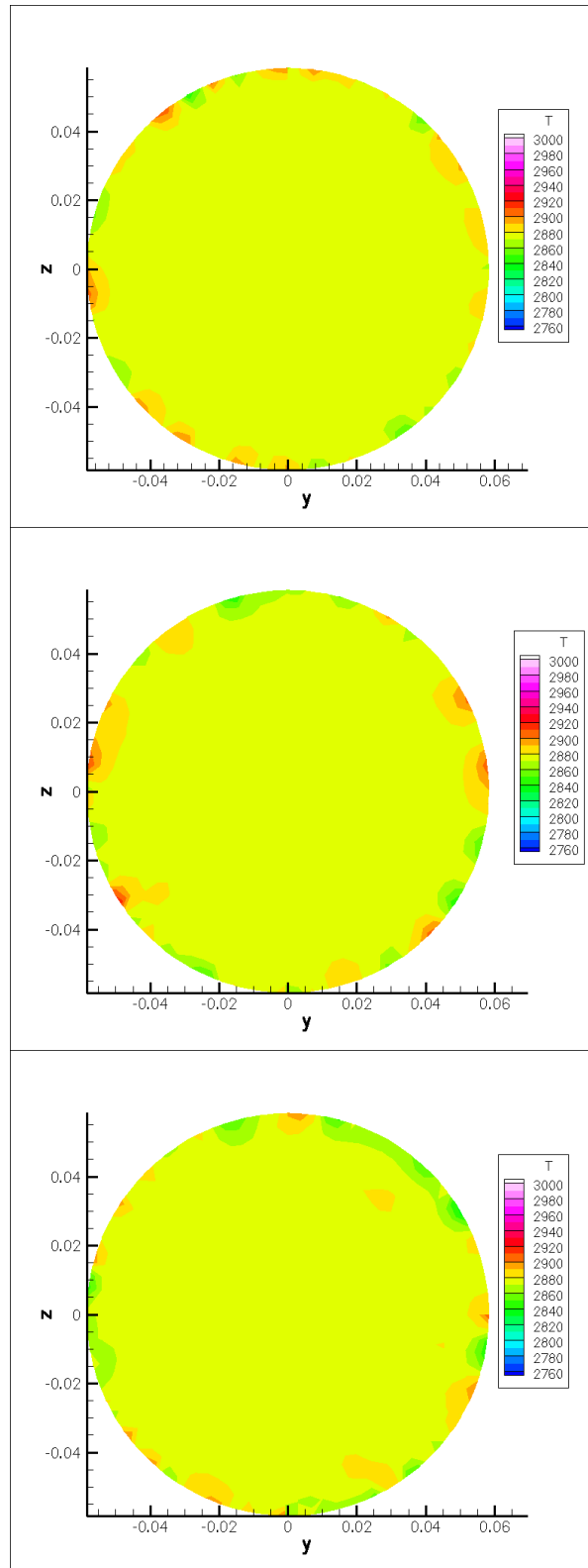
Figure 10: Temperature contours at x = 0.2 m for BATES 15 lb. motor with injection conditions defined by P82. Time: 0.5s, 1.0s, 1.5s (top to bottom).
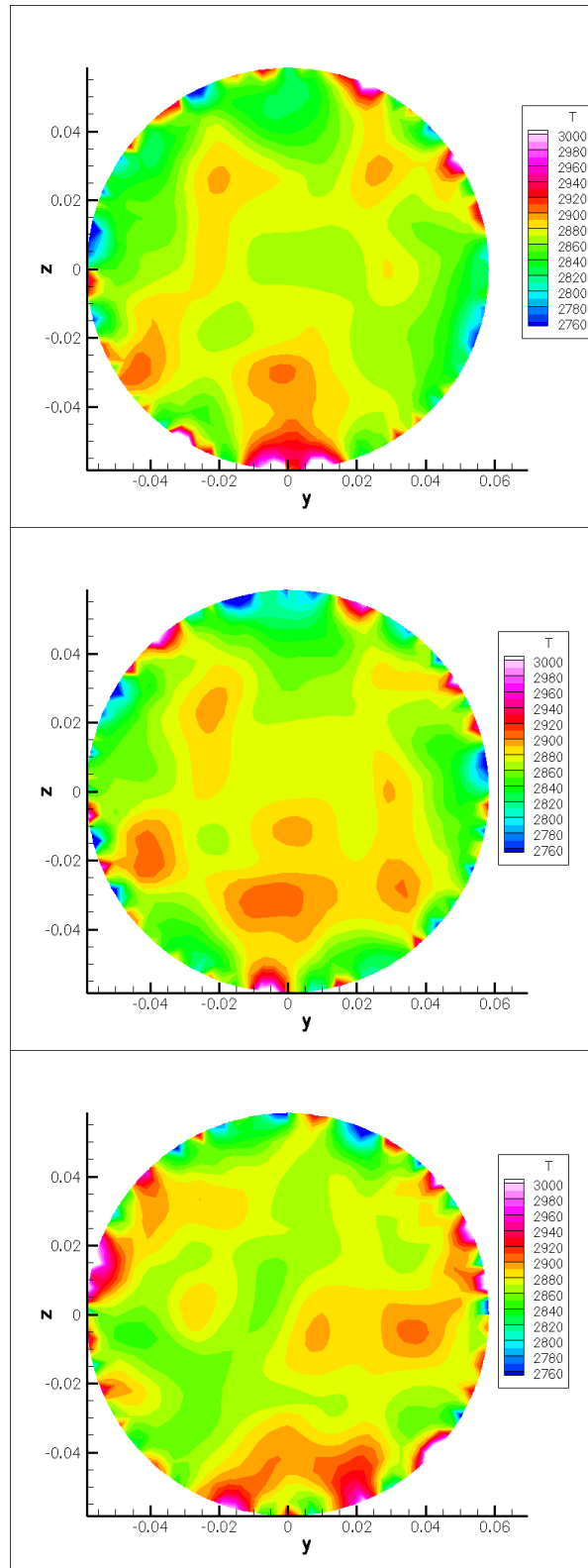
Figure 11: Temperature contours at x = 0.2 m for BATES 15 lb. motor with injection conditions defined by PBMOD. Time: 0.5s, 1.0s, 1.5s (ltop to bottom).
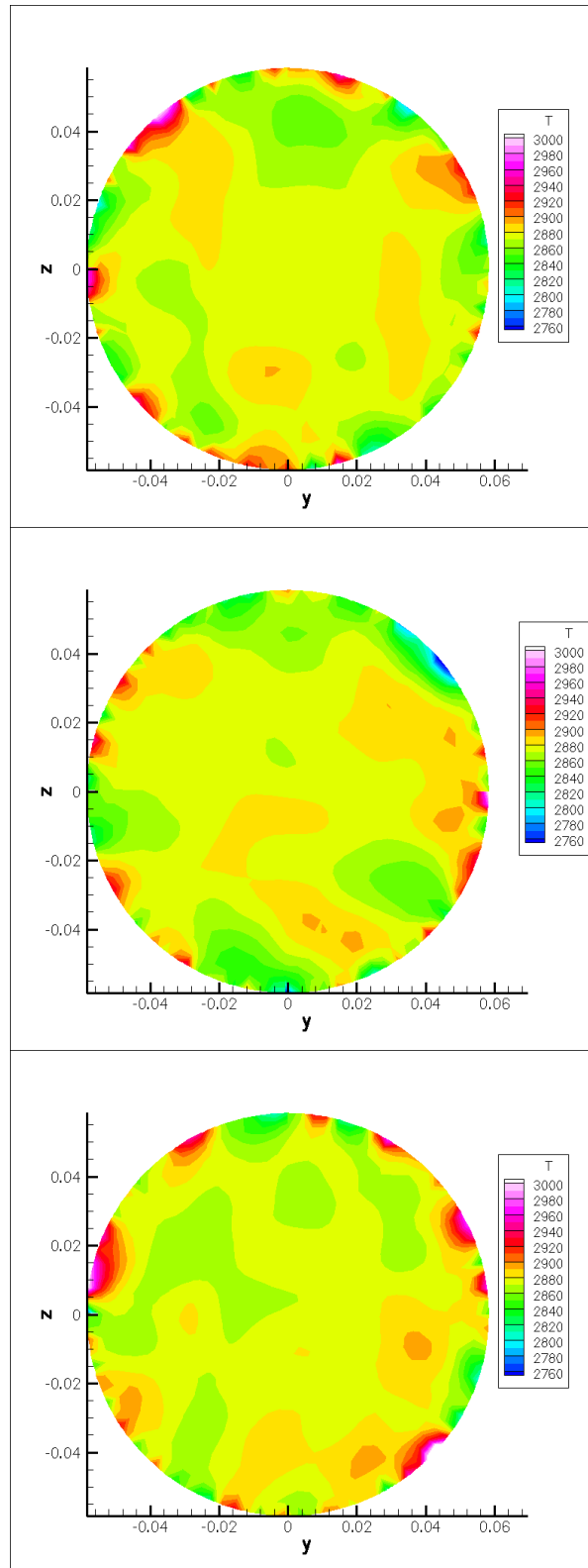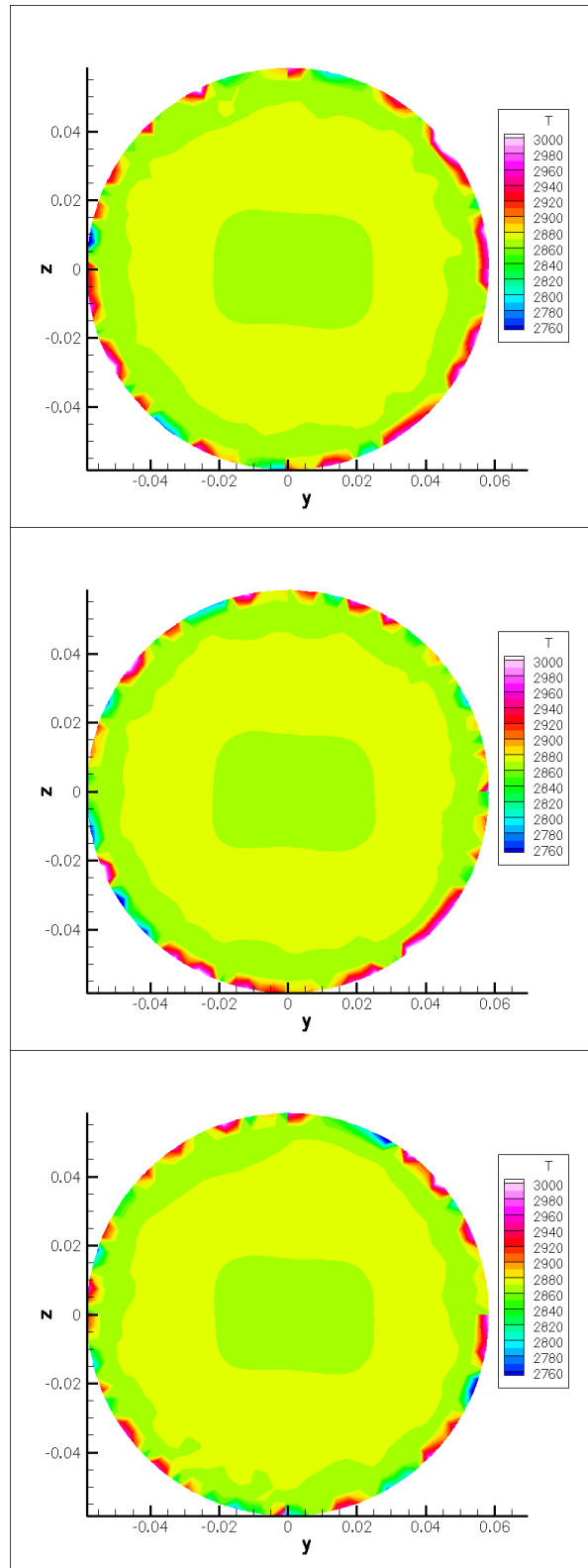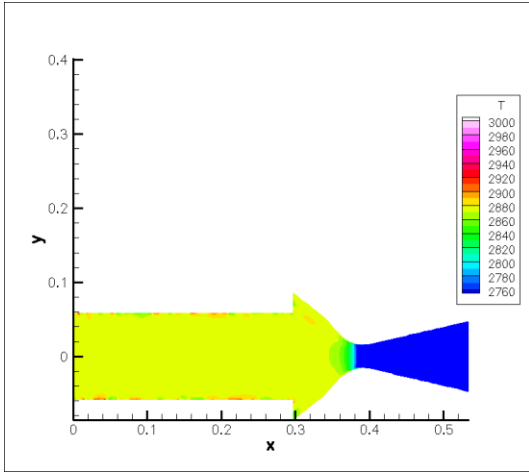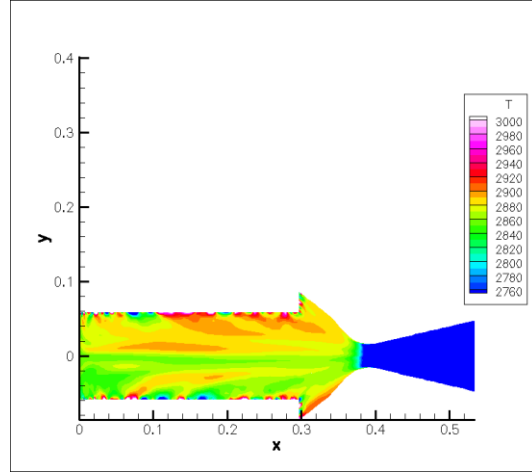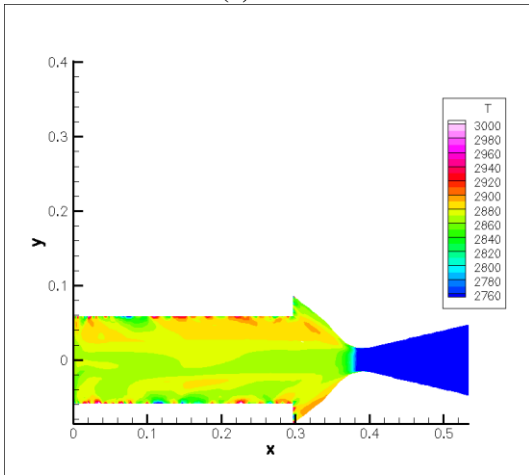
Figure 12: Temperature contours at x = 0.2 m for BATES 15 lb. motor with injection conditions defined by M24. Time: 0.5s, 1.0s, 1.5s (top to bottom).

Figure 13: Temperature contours at x = 0.2 m for BATES 15 lb. motor with injection conditions defined by White Noise 10%. Time: 0.5s, 1.0s, 1.5s (top to bottom).
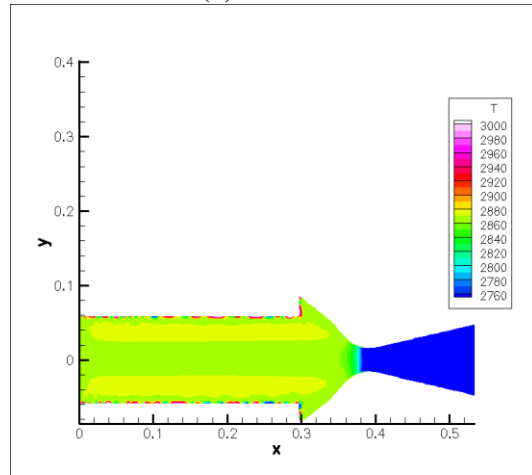
(a) P82

(b) PBMOD

(c) M24

(d) White noise 10%

Figure 14: Temperature contours at z = 0m at t = 1.0s for BATES 15 lb. motor.

5 Bates 70 lb. Motor Results

5.1 Acoustics

The larger 70 lb. BATES motor was also simulated to ensure that the results gained from the simulation of the 15 lb. motor was replicated on a larger scale. The computational cost of the larger grid allowed for only the white noise and the PBMOD cases to be run. Figure 15 shows the head end pressure history as a function of time from 0.5 seconds to 1.5 seconds for the case with PBMOD propellant. The average headend pressure is 6.9871 MPa.

An examination of the FFT's presented by Figure 16 show some similarities to the results that were found for the BATES 15 lb motor. One difference is that the FFT of the case using the white noise propellant shows little differentiation in amplitude throughout the entire range of frequency. This occurs because of the sampling rate used to record the pressure at the head-end of the motor. This same effect was observed with the 15 lb. motor, but was remedied by increasing the sampling rate from every 0.1ms to 0.01ms. Computational cost of the running the larger motor has prohibited doing this for the 70 lb. motor. Despite the lack of clearly defined acoustic modes, this plot is still useful in examining the amplitude characteristics for the white noise FFT.

At larger frequencies, the longitudinal modes of the PBMOD case are clearly visible due to a large increase in amplitude at these frequencies. The theoretical values and the calculated values from the white noise and PBMOD simulations may be seen in Table 4. It can also be seen that the amplitude of these peaks decreases with increasing mode number. In comparison, and matching what was seen in the BATES 15 lb results, the white noise case has relatively constant amplitude that does not change as the mode number increases. The amplitudes of the first, second, and third modes in the white noise case are much smaller than that of the PBMOD case. The amplitude of the first mode of the PBMOD case is about 16 times larger than the amplitude of the first mode of the white noise case. This difference in amplitude begins to decrease when moving to higher modes; however the amplitude of the second mode for the PBMOD case is still about 6 times higher than the amplitude of the white noise case. These differences are even more pronounced than what was seen in the BATES 15 lb. runs where the differences between

the PBMOD and the white noise amplitudes were only about 160% for the first mode and 110% for the second mode.

The results from the BATES 70 lb. motor are encouraging in that they are similar to what was found in the 15 lb. motor. This shows that the acoustic modes found in the FFT plots from the 15 lb. motor at the acoustic modes are not just a product of the computational grid for the motor. Similar results showing the difference between white noise and actual propellant models are gained by simulating the two different sizes of BATES motors. This suggests that other types of motors will be similarly affected by the choice of propellant model.

5.2 Chamber Flow Dynamics

As what was done for the BATES 15 lb. motor, the temperature contour plots of the BATES 70 lb. motor in Figure 17 and Figure 18 show the differences between the white noise and PBMOD simulations. The white noise plots show temperature fluctuation at the edges of the motor chamber but a constant temperature within the chamber. The PBMOD defined propellant creates temperature fluctuation around the edge of the chamber, but it also has varying temperature within the chamber. For both cases, the most extreme temperature differences are found near the burning surface at the chamber edge.

The plots in Figure 19 show the temperature contour through the entire chamber of the motor. Once again, although the white noise case shows fluctuation near the edge of the chamber, it fails to capture the temperature fluctuation that is seen on the interior of the chamber. The motor that used the bimodal propellant model shows that there is the most fluctuation near the boundaries of the motor, and it also shows fluctuation within the chamber itself as was seen in the Bates 15 lb. motor.
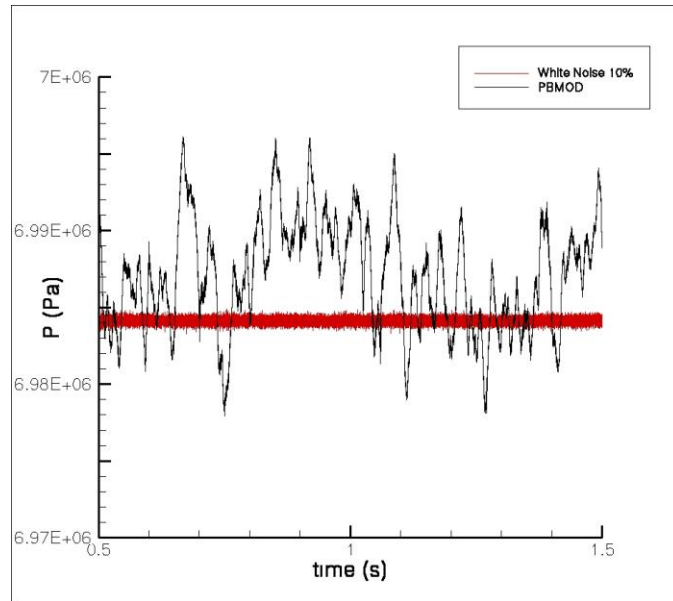
5.3 Figures and Tables

Figure 15: Time history of the head end pressure for the 70lb. BATES motor with PBMOD and white noise propellant.
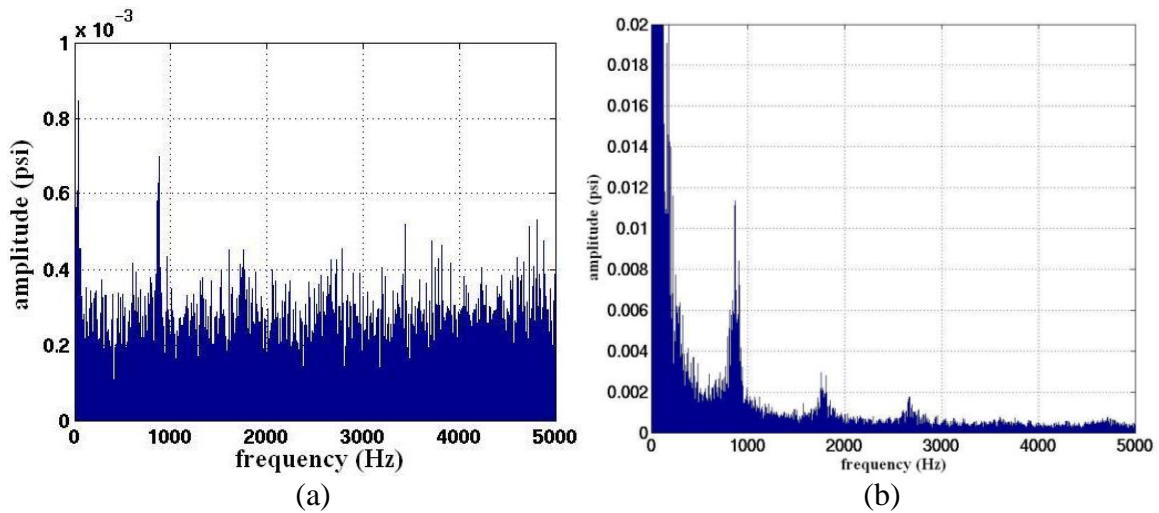

| (a) | (b) |

Figure 16: FFT plots for head end pressure of the Bates 70lb. motor. (a) White noise (b) PBMOD

Table 4: Computed and theoretical frequencies of the first three longitudinal modes for the Bates 70lb. motor.

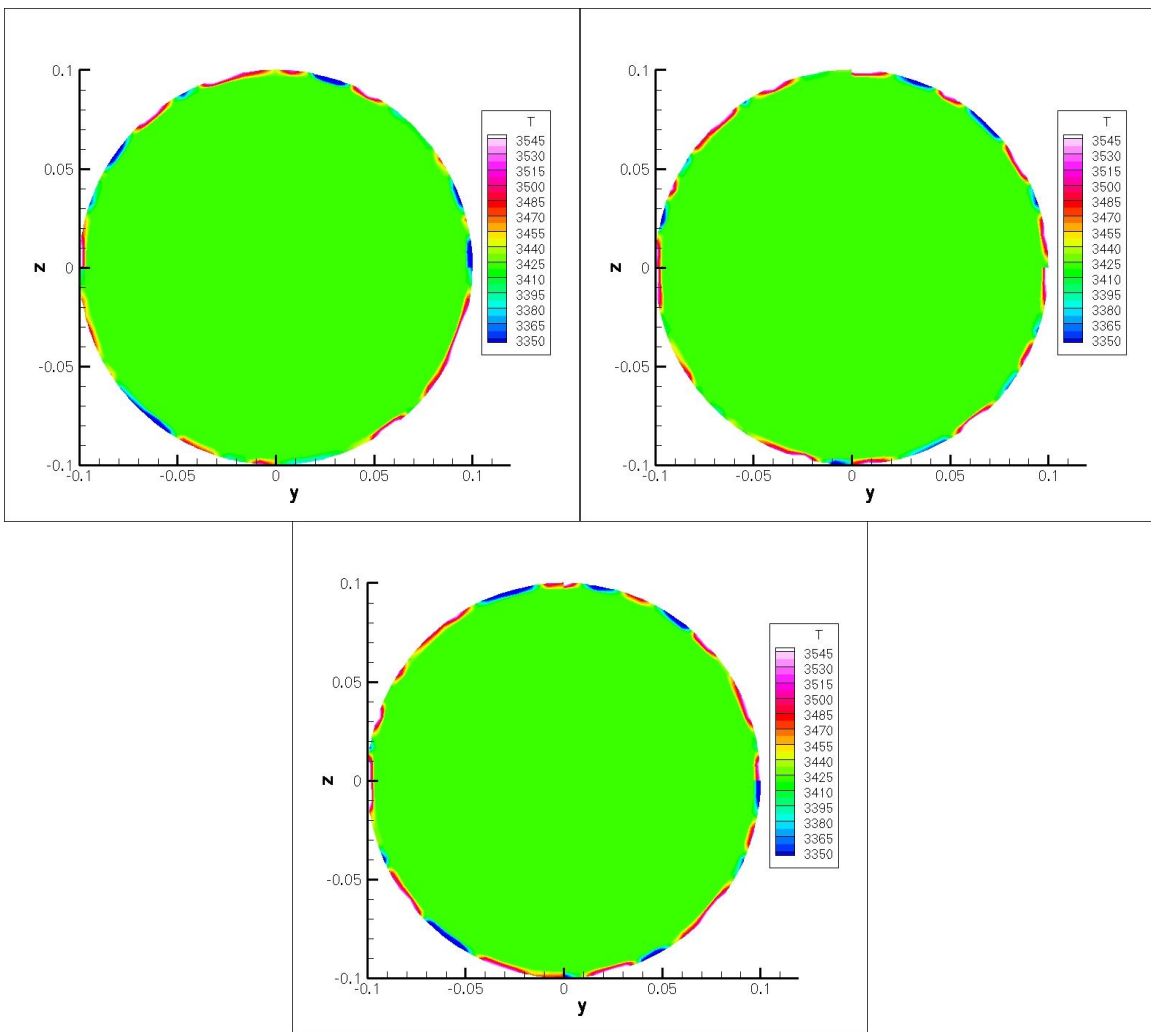| Longitudinal Mode	1			2			3		
	Hz	Pa	Psi	Hz	Pa	psi	Hz	Pa	Psi
Theoretical	815	---	---	1629	---	---	2444	---	---
White Noise	878	4.82	6.99E-4	1751	3.12	4.53E-4	2777	3.13	4.54E-4
PBMOD	866	78.30	0.0114	1755	20.23	0.00293	2668	11.95	0.00173

Figure 17: Temperature contours at x = -0.5 m for BATES 70 lb. motor with injection conditions defined by White Noise 10%. Time: 0.5s, 1.0s, 1.5s (left to right, top to bottom).
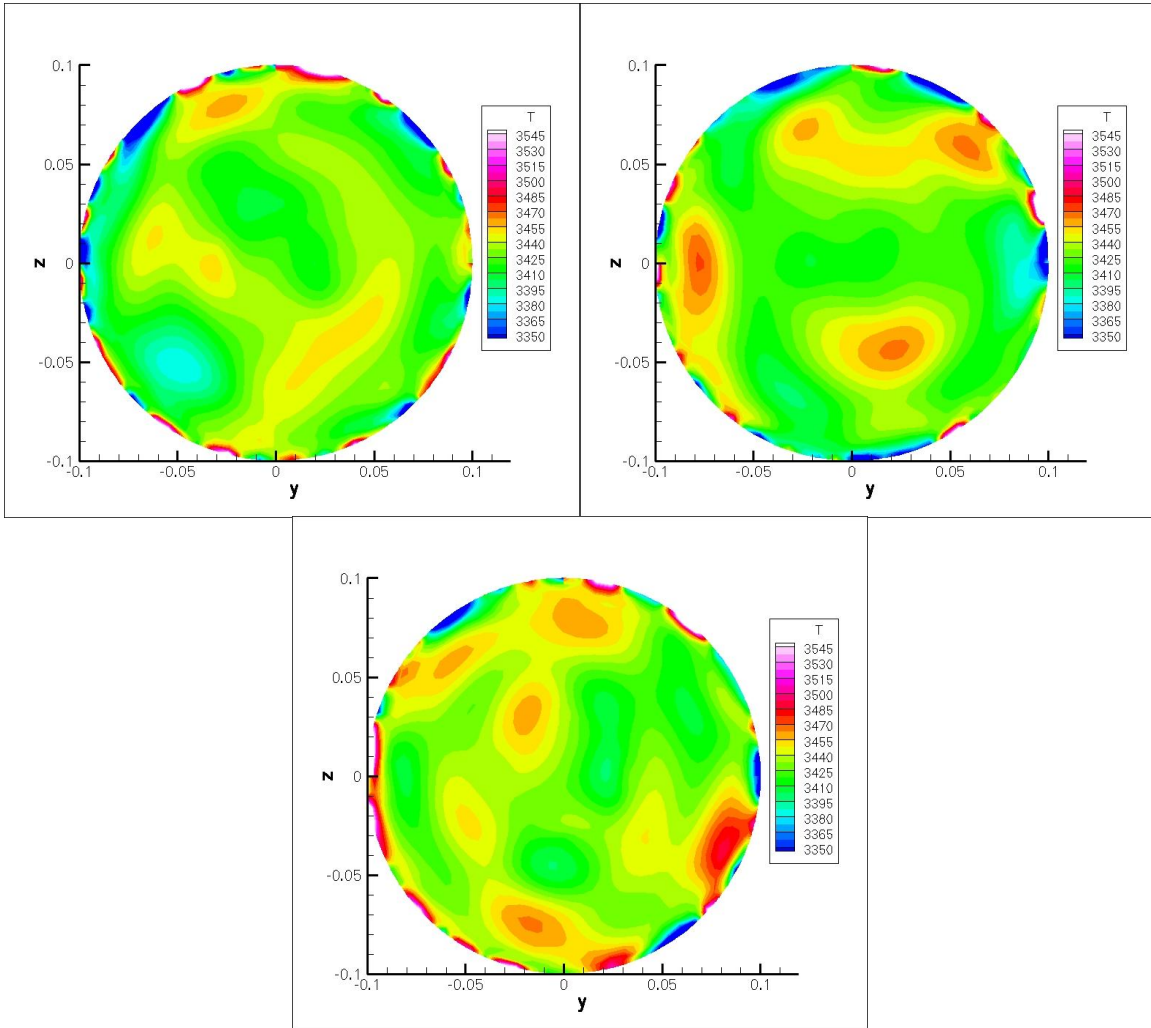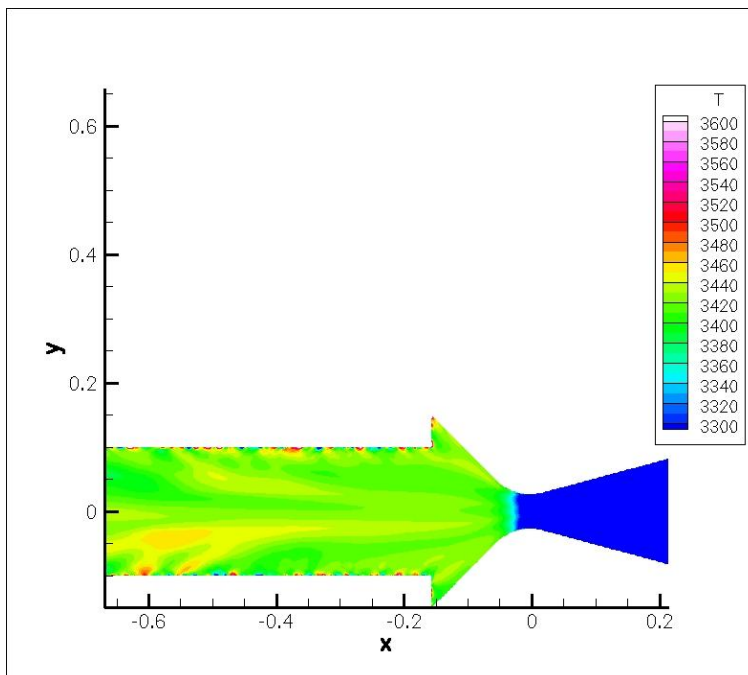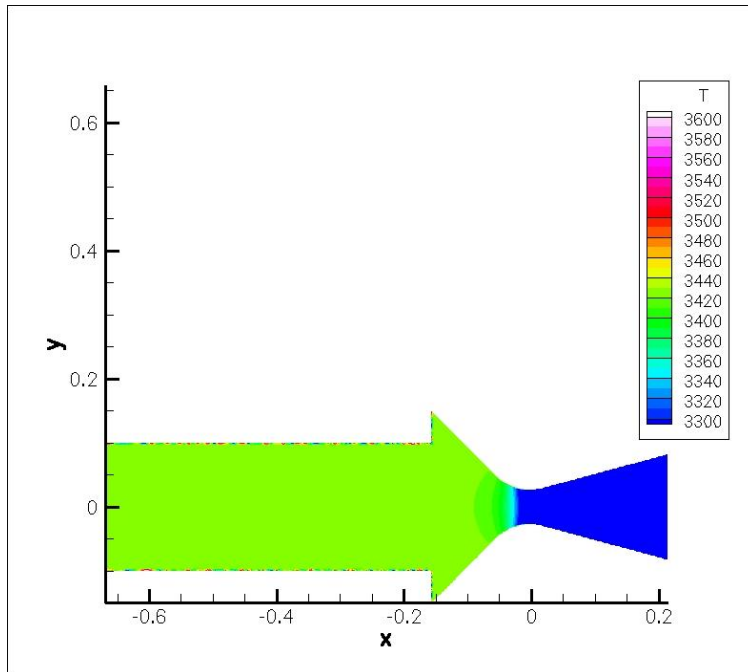
Figure 18: Temperature contours at x = -0.5 m for BATES 70 lb. motor with injection conditions defined by PBMOD. Time: 0.5s, 1.0s, 1.5s (left to right, top to bottom).

Figure 19: Temperature contours at z = 0 m at t = 1.5s for BATES 70 lb. motor. Top: White Noise Bottom: PBMOD.

6 Future Work

A portion of this study that could use future investigation is revealed by an examination of the FFT plots shown in Figure 9. There are unexpectedly high amplitudes in the low frequency range. For the propellant model simulations, the acoustic modes are clearly evident; however, the amplitude of these modes is minimal when compared to the amplitude shown near 0 Hz. This is a point of concern as such high amplitude low frequency content is unexpected and thought to be a result of calculation method. One theory is that high amplitudes at these low frequencies are a consequence of the random walk process that is used to predict the propellant covariance values past what was produced by Rocfire. The Rocfire simulations take a large amount of computational time, so initial results were gathered, and then forecasting was used to predict up to the amount of time needed for the burning simulation. The random walk prediction method could produce mean values for velocity and temperature that could change from the mean gathered from the actual simulation values. This may or may not be a significant factor to the problems that were encountered in the initial simulations, but it seems plausible enough to warrant being fixed.

The initial Rocfire results contained too little data to be able to compare with forecasting models for accuracy, so one solution to this problem is to run Rocfire to the same amount of time for which the motor simulation will run, so that an exact solution can be created. This exact solution can then be used in place of forecasting to determine the injection boundary conditions. It can also be used as a guide for future attempts to create an accurate forecasting model if forecasting is found to be the reason for the large amplitudes at small frequencies.

Despite the issues with the low frequency amplitudes, the results from the higher frequency portion of the FFT give a basis to the fact that modeling propellant morphology to create boundary injection conditions can have a significant effect on the chamber flow and acoustic nodes. The preliminary results from this study encourage the further study of the modeling of the propellants for boundary conditions in order to enhance the accuracy of solid rocket simulations.

7 Conclusions

The velocity-temperature temporal fluctuations above a propellant have been previously described and calculated in an entirely two-dimensional case [19]. It was determined in this study that these fluctuations have an effect on chamber flow, specifically head end pressure. However, these tests have never been run in three dimensions; therefore, it was necessary to test the conclusions of the previous work using a three-dimensional simulation of an actual test rocket. This study has shown the effects of propellant modeling on the simulation of the burning of the BATES motor using three different propellant morphologies.

The results of this numerical simulation revealed the dependence of the amplitudes of the longitudinal acoustic modes and the internal chamber flow dynamics on the propellant morphology. FFT analysis of the head end pressure time history clearly exhibited the acoustic modes while also showing that changing the propellant could increase or decrease the amplitude of these modes. The amplitudes for the acoustic modes when using the PBMOD propellant was consistently larger than that of the M24 or P82 propellants. Furthermore, the amplitudes of the acoustic modes from the propellant defined boundary conditions were characteristically different than that of the white noise defined boundary case. The white noise case showed much lower amplitude at the first acoustic mode than was seen in the propellant cases. Also, the propellant cases showed greater decrease in amplitude as the frequency of the mode increased compared to what was seen with white noise. The chamber temperatures were also plotted as contours to provide further comparison between the propellants and the white noise. All of the cases showed the greatest fluctuation near the edges of the motor; however, the propellants also showed fluctuation within the interior of the chamber while this fluctuation was not evident in the white noise case. These comparisons have shown that using white noise as a model propellant is a poor approximation, especially when actual propellant morphologies are available for use.

This study has opened up a few areas where future investigation could be considered. The propellant morphology cases demonstrated high amplitudes in the head

end pressure FFTs near the small frequency range that is thought, at least in part, to be a result of artificial creation through the calculation of forecasted values. Either a new forecasting method or a longer simulation of the burning propellant is necessary to test this hypothesis, so that a more accurate solution is found for the low frequency amplitudes. Also, the BATES motor represents a relatively small test motor, so it would be interesting to see how propellant morphology would affect larger rockets that have lower frequency acoustic modes. The extension of this study to simulations of larger motors will only improve the understanding of the effects of propellant morphology and help reveal its consequences on actual rockets and manned space flight. Further study in this area could provide ways to improve and optimize efficiency and rocket performance.

References

1. Najjar, F.M., Massa, L., Fiedler, R., Haselbacher, A., Wasistho, B., Balachandar, S., & Moser, R.D. Effects of aluminum propellant loading and size distribution in BATES motors: A multiphysics computational analysis. AIAA Paper No. 2005-3997, July 2005.
2. Najjar, F.M., Ferry, J.P., Haselbacher, A., & Balachandar, S. Simulations of solid-propellant rockets: Effects of aluminum droplet size distribution. *J. Spacecraft & Rockets* **43** (2006), pp. 1258-1270.
3. Blomshield, F.S. Historical perspective of combustion instability in motors: Case studies. AIAA Paper No. 2001-3875, July 2001.
4. Telara, M., Spa, A., Stella, F., Paglia, F., Giagi, M. Pressure oscillations in solid rocket motors. *Fluent News* Fall 2005, pp. S14-S16.
5. Lupoglazoff, N., Vuillot, F. Parietal vortex shedding as a cause of instability for long solid propellant motors – numerical simulations and comparisons with firing tests. AIAA Paper No. 96-0761, January 1996.
6. Flandro, G., Jacobs, H. Vortex generated sound in cavities. AIAA Paper No. 73-1014, October 1973.
7. Lupoglazoff, N., Vuillot, F. Numerical simulation of vortex shedding phenomenon in 2D test case solid rocket motors. AIAA Paper 92-0776, January 1992.
8. Kourta, A. Computation of vortex shedding in solid rocket motors using time-dependent turbulence model. *J. Propulsion and Power* **15** 3 (1999), pp. 390-400.
9. Kourta, A. Instability of channel flow with fluid injection and parietal vortex shedding. *Computers & Fluids* **33** (2004), pp. 155-178.
10. Volkov, K.N., Emel'yanov, V.N. Turbulent flows in channels with injection. Results of large eddy simulation and the two equation turbulence model. *Fluid Dynamics* **43** 4 (2008), pp. 573-582.
11. Ciucci, A., Iaccarino, R., Moser, R., Najjar, F., Durbin, P. Simulation of rocket motor internal flows with turbulent mass injection. Center for Turbulence Research, Stanford Univ. (1998), pp. 245-266
12. Apte, S., Yang, V. Unsteady flow evolution in porous chamber with surface mass injection, part 1: Free oscillation. *AIAA Journal.* **39** 80 (2001), pp. 1577-1586.
13. Glick, R. Private communication.
14. Culick, F.E.C. Unsteady motions in combustion chambers for propulsion systems. RTO AGARDograph, AG-AVT-039 (2006).
15. Flandro, G. Vortex driving mechanism in oscillatory rocket flows. *J. Propulstion and Power* **2** 3 (1986), pp.206-214.
16. Massa, L., Jackson, T.L., Buckmaster, J., & Najjar, F. Fluctuations above a burning heterogeneous propellant. *Journal Fluid Mechanics* **581** (2007), pp. 1-32.
17. Atwood, ?., Maggi, F. Private communications.
18. Beckstead, M.W., Derr, R.L., Price, C.F. Model of composite solid-propellant combustion based on multiple flames. AIAA Journal **8** 12 (1970), pp. 2200-2207.
19. Jackson, T.L, Buckmaster, J. Heterogeneous propellant combustion. *AIAA Journal* **40** 6 (2002), pp. 1122 -1130.
20. Knott, G. M., Jackson, T.L., Buckmaster, J. Random packing of heterogeneous propellants. *AIAA Journal* **39** 4 (2001), pp. 678-686.
21. Kochevets, S., Buckmaster, J., Jackson, T.L., Hegab, A. Random packs and their use in modeling heterogeneous solid propellant combustion. *J. Propulsion and Power* **17** 4 (2001), pp. 883-891.
22. Maggi, F., Stafford, S., Jackson, T.L., Buckmaster, J. Nature of packs used in propellant modeling. *Physical Review E* **77** (2008), pp.1-17.
23. Chen, M., Buckmaster, J., Jackson T.L., Massa, L. Homogenization issues and the combustion of heterogeneous solid propellants. *Proc. Combust. Inst.* **29** (2002), pp. 2923-2929.
24. Daimon, Y., Jackson, T.L., Topalian, V., Freund, J.B., Buckmaster, J. Effect of propellant morphology on acoustics in a planar motor. *Theoretical Computational Fluid Dynamics* **23** (2009), pp. 63-77.
25. R.L. Geisler, & C.W. Beckman. "The History of the BATES Motors at the Air Force Rocket Propulsion Laboratory", AIAA Paper No. 98-3981, 1998.
26. Winkler, Robert L., & Hays, William L. Statistics: Probability, Inference, and Decision. 2nd Edition. Holt, Rinehart and Winston: New York, 1975.